

Discovery of a Fast Iron Low-ionization Outflow in the Early Evolution of the Nearby Tidal Disruption Event AT 2019qiz

TIARA HUNG,¹ RYAN J. FOLEY,¹ S. VEILLEUX,^{2,3} S. B. CENKO,^{4,3} JANE L. DAI,⁵ KATIE AUCHETTL,^{6,7,1} THOMAS G. BRINK,⁸ GEORGIOS DIMITRIADIS,¹ ALEXEI V. FILIPPENKO,⁸ S. GEZARI,^{2,3} THOMAS W.-S. HOLOIEN,^{9,*} CHARLES D. KILPATRICK,¹ BRENNA MOCKLER,¹ ANTHONY L. PIRO,¹⁰ ENRICO RAMIREZ-RUIZ,^{1,11} CÉSAR ROJAS-BRAVO,¹ MATTHEW R. SIEBERT,¹ SJOERT VAN VELZEN,^{2,12} AND WEIKANG ZHENG⁸

¹Department of Astronomy and Astrophysics, University of California, Santa Cruz, California, 95064, USA

²Department of Astronomy, University of Maryland, College Park, MD 20742, USA

³Joint Space-Science Institute, University of Maryland, College Park, MD 20742, USA

⁴Astrophysics Science Division, NASA Goddard Space Flight Center, MC 661, Greenbelt, MD 20771, USA

⁵Department of Physics, University of Hong Kong, Pokfulam Road, Hong Kong

⁶School of Physics, The University of Melbourne, Parkville, VIC 3010, Australia

⁷ARC Centre of Excellence for All Sky Astrophysics in 3 Dimensions (ASTRO 3D), Australia

⁸Department of Astronomy, University of California, Berkeley, CA 94720-3411, USA

⁹The Observatories of the Carnegie Institution for Science, 813 Santa Barbara St., Pasadena, CA 91101, USA

¹⁰The Observatories of the Carnegie Institution for Science, 813 Santa Barbara Street, Pasadena, CA 91101, USA

¹¹DARK, Niels Bohr Institute, University of Copenhagen, Lyngbyvej 2, 2100 Copenhagen, Denmark

¹²Center for Cosmology and Particle Physics, New York University, NY 10003, USA

Submitted to ApJ

ABSTRACT

We report the results of UV and optical photometric and spectroscopic analysis on the tidal disruption event (TDE) AT 2019qiz. Our follow-up observations started shortly after ($\lesssim 10$ days) its optical light begin to rise and lasted for a period of six months. Our late-time host-dominated spectrum indicates that the host galaxy likely harbours a weak AGN. The initial *HST* spectrum of AT 2019qiz exhibits a iron and low-ionization broad absorption line (FeLoBAL) system that is seen for the first time in a TDE. This spectrum also bears a striking resemblance to that of Gaia16apd, a superluminous supernova. Our observations provide insights into the outflow properties in TDEs and show evidence for a connection between TDEs and engine-powered supernovae at early phase, as originally suggested in Metzger & Stone (2016). In a time frame of 50 days, the UV spectra of AT 2019qiz started to resemble previous TDEs with only high-ionization BALs. The change in UV spectral signatures is accompanied by a decrease in the outflow velocity, which began at $15,000 \text{ km s}^{-1}$ and decelerated to $\sim 10,000 \text{ km s}^{-1}$. A similar evolution in the H α emission line width further supports the speculation that the broad Balmer emission lines are formed in TDE outflows. In addition, we detect narrow absorption features on top of the FeLoBAL signatures in the early *HST* UV spectrum of AT 2019qiz. The measured H I column density corresponds to a Lyman-limit system whereas the metal absorption lines, such as N V, C IV, Fe II, and Mg II, are likely probing the circumnuclear gas and interstellar medium in the host galaxy.

Keywords: accretion, accretion disks – black hole physics – galaxies: nuclei – ultraviolet: general

1. INTRODUCTION

Corresponding author: Tiara Hung
 tiarahung@ucsc.edu

* NHFP Einstein Fellow

Tidal disruption events (TDEs) refer to the transient phenomenon where a star on a close passage to a supermassive black hole (SMBH) is torn apart under tidal stress (Hills 1975). For a star that initially travelled on

a parabolic orbit, the disruption unbinds about half of the stellar mass while the bound other half assembles into an accretion disk and feeds the black hole until the debris streams are drained. In scenarios where disk formation is efficient, the onset of accretion resulting from a TDE is set by the fallback time (t_{fallback}), which corresponds to the time it takes for the most bound debris on highly eccentric orbits to return to the pericenter (e.g. $t_{\text{fallback}} = 41M_{\text{BH},6}^{1/2}$ days; [Lodato et al. 2009](#)). The liberation of gravitational potential energy of the infalling gas is then converted to radiation across the electromagnetic spectrum, thus allowing a TDE to be detected by the observers ([Frank & Rees 1976](#); [Rees 1988](#)).

Observationally, X-ray, UV, and optical sky surveys have identified nearly 5 dozens of TDEs (e.g. [Komossa & Bade 1999](#); [Komossa & Greiner 1999](#); [Esquej et al. 2007](#); [Levan et al. 2011](#); [Gezari et al. 2012](#); [Holoien et al. 2016](#); [van Velzen et al. 2020a](#)). However, these events, depending on the wavelength of discovery, exhibit a dichotomy in their properties. While the X-ray-detected TDEs are characterized by thermal emission that is consistent with the accretion model, most optically-detected TDEs appear to lack or have very weak ($\lesssim 10^{-2}L_{\text{UV}}$) X-ray emission (e.g. [Holoien et al. 2019a](#); [van Velzen et al. 2019, 2020b](#)). In particular, the optically-detected events tend to have cooler temperatures that are 1–2 orders of magnitude lower than their X-ray counterparts ([van Velzen et al. 2011](#); [Arcavi et al. 2014](#); [Holoien et al. 2014](#); [Hung et al. 2017](#)). The optical TDEs are also able to maintain roughly the same temperature over a timescale of months.

The discrepancy between the two observational population of TDEs may arise from the biggest uncertainty in the current TDE framework, which is whether the stellar debris can circularize efficiently following a TDE. Circularization requires the bound debris in highly eccentric orbits to lose a large amount of orbital energy to form a circular disk at $2R_p$ (conservation of specific angular momentum). In the classical scheme, the energy is dissipated efficiently via shocks produced by self-intersection at the pericenter ([Evans & Kochanek 1989](#); [Rees 1988](#); [Phinney 1989](#)). This assumption is challenged by recent simulations and analytical calculations that find circularization to be extremely inefficient in certain regions of the parameter space ([Dai et al. 2015](#); [Shiokawa et al. 2015](#); [Hayasaki et al. 2016](#); [Bonnerot et al. 2016](#); [Svirski et al. 2017](#)). This possibility lays the foundation for an alternative mechanism in which the UV and optical emission in TDEs is powered by the stream-stream collision shocks ([Shiokawa et al. 2015](#); [Piran et al. 2015](#)). However, this model naturally leads to a slower light curve evolution, which is at odds with the observations

where several TDEs closely follow the $t^{-5/3}$ decline as predicted for the mass fallback rate ([Metzger & Stone 2016](#)).

In TDEs where disk formation is efficient and where radiation is driven by the inner accretion flows, a reprocessing layer at 10–100 R_T is often invoked to explain the cooler temperature in optical TDEs. Some works suggest that the bound debris could build up a hydrostatic envelope around the SMBH to reprocess the X-ray/EUV radiation released by accretion ([Loeb & Ulmer 1997](#); [Guillochon & Ramirez-Ruiz 2013](#)) while others suggest that outflows could be the major reprocessing material in TDEs ([Miller 2015](#); [Metzger & Stone 2016](#)). Indeed, radiation-driven winds are a natural consequence of TDEs given that the “super-Eddington” phase should be common among stellar disruptions by $M_{\text{BH}} \lesssim 10^7 M_{\odot}$ black holes ([Strubbe & Quataert 2009](#); [Wu et al. 2018](#))

Multi-wavelength follow-up observations of TDEs have detected winds across a wide range of velocities. X-ray observations of ASASSN-14li revealed highly ionized outflows moving at both low and high velocities, from a few $\times 100$ km s $^{-1}$ to $0.2c$ ([Miller et al. 2015](#); [Kara et al. 2018](#)). The UV spectrum of ASASSN-14li also shows signs of a low velocity outflow ([Cenko et al. 2016](#)), which has a similar velocity to the slower X-ray gas found by [Miller et al. \(2015\)](#). In the same event, radio observations are also supportive of the presence of either a sub-relativistic outflow ([Alexander et al. 2016](#)) or an off-axis relativistic jet ([van Velzen et al. 2016](#)). Including AT 2019qiz, the subject of this paper, blueshifted broad absorption lines (BALs) that correspond to outflow velocities of 5,000 – 15,000 km s $^{-1}$ are detected in 4 out of 5 TDEs with HST UV follow-up spectroscopy with the exception of ASASSN-14li ([Brown et al. 2018](#); [Blagorodnova et al. 2019](#); [Hung et al. 2019](#)). Orientation effects may explain why BALs are absent in some TDEs ([Parkinson et al. 2020](#)).

Contrary to the late-time observational properties of TDEs, which tend to be more uniform as the reprocessing layer becomes transparent and allows one to probe the accretion disk directly ([Jonker et al. 2020](#); [van Velzen et al. 2018](#)), early-time observations are expected to exhibit a higher degree of diversity in the flare properties. Early multi-wavelength observations of TDEs are critical for understanding debris stream evolution and super-Eddington accretion in TDEs though they have rarely been obtained. To date, there are only a handful of TDEs with published pre-peak multi-band light curves (e.g. ASASSN-18pg and ASASSN-19bt; [Holoien et al. 2020, 2019b](#)). Among these, ASASSN-19bt has the most densely-sampled rising optical light curve as it is located in the TESS Continuous Viewing Zone.

AT 2019qiz is the most well-observed TDE with a wealth of early-time multi-wavelength data since ASASSN-19bt. Here we present the analysis on the UV and optical data of AT 2019qiz, the current record holder of the nearest TDE. We note that (Nicholl et al. 2020, hereafter N20) also analyzed the evolution of UV and optical broadband photometry and optical spectroscopy of AT 2019qiz. However, our analysis has a stronger focus on the unique multi-epoch *HST* UV spectra that have not been reported before. In addition, our *ugri* light curves were obtained independently at a higher cadence than N20 at early times.

This paper is structured as follows. We describe the observations, including photometry and spectroscopy at UV and optical wavelengths, in section 2. We present the procedures and results of our analysis in section 3. Specifically, we detail the evolution and the identification of broad and narrow UV absorption lines in the *HST* spectra in section 3.3. We discuss the implications of our results and the origin of the UV absorption lines in section 4. Our conclusions are presented in section 5.

2. OBSERVATIONS AND DATA REDUCTION

AT 2019qiz is a fast-evolving nuclear transient in a nearby galaxy ($z = 0.0151$) 2MASX J04463790-1013349. It was first discovered by the ATLAS on Sep 18 2019 in the orange filter and subsequently by the Zwicky Transient Facility (ZTF) on Sep 19 2019 in the r filter thus also named as ATLAS19vfr and ZTF19abzrhgq. The most recent pre-flare non-detection was provided by ZTF on Sep 16 2019 with an upper limit of $g > 19.22$ mag. We classified AT 2019qiz as a TDE from a Keck LRIS spectrum obtained on Sep 25 2019 (Siebert et al. 2019) while still on the rise. Given the proximity of the TDE and the early classification, multi-wavelength follow-up observations have been triggered by the science community. Notably, AT 2019qiz was reported to be detected at radio frequencies and rising in October and November 2019 (ATel #13334).

We detail the follow-up observations that are analyzed in this paper in the subsections that follow. Throughout the paper, we adopt a flat Λ CDM cosmology with $H_0 = 67.4$ km s $^{-1}$ Mpc $^{-1}$ and $\Omega_m = 0.315$ measured by the Planck mission (Planck Collaboration et al. 2020). The time difference (Δt) is expressed in rest-frame time with respect to the peak of g -band light curve at MJD 58763.93.

The *Swift* Ultraviolet Optical Telescope (UVOT; Gehrels et al. 2004; Roming et al. 2005) monitoring of AT 2019qiz is simultaneously accompanied by observations with the *X-ray Telescope* (XRT) onboard the Neil Gehrels *Swift* Observatory. The X-ray emission in

AT 2019qiz peaks around $\approx 10^{41}$ erg s $^{-1}$ in the 0.3–10keV band, which is 2–3 orders of magnitude weaker than the UV and optical emission (N20). Given that the *Swift* XRT data set has already been analyzed in N20 and is independent from our other analysis, we reference their reported luminosity and hardness ratio where appropriate without repeating the data reduction and analysis in this work.

All data for AT 2019qiz have been corrected for Milky Way foreground extinction assuming a Cardelli et al. (1989) extinction curve with $R_V = 3.1$ and $E(B - V) = 0.0939 \pm 0.0088$ mag (Schlafly & Finkbeiner 2011).

2.1. *HST STIS spectra*

We obtained 3 epochs of UV spectra of AT 2019qiz with *HST* STIS (GO-16026; PI Hung) on 2019 October 21, 2019 December 12, and 2020 January 15. The spectra were obtained through a $52'' \times 0''.2$ aperture. For the near-UV (NUV) and far-UV (FUV) MAMA detectors, the G140L and G230L gratings were used in order to cover the spectral range of 1150–1730 Å and 1570–3180 Å at resolutions of 1.2 Å and 2.2 Å, respectively. During the first two visits, the observation was obtained over a single *HST* orbit, with three equal exposures of 170 s in the NUV and three equal exposures of 335 s in the FUV. The observations obtained in the last visit consists of three 692 s exposures in the NUV and three 876 s exposures in the NUV, totaling two *HST* orbits. We used inverse-variance weighting method to combine the 1-dimensional spectra of the same epoch that were output by the *HST* pipeline.

2.2. *Optical Photometry*

Following the classification of AT 2019qiz as a TDE on $\Delta t = -13$ days, we triggered photometric and spectroscopic monitoring spanning about 6 months in time (between September 2019 and March 2020) before the TDE became too faint and Sun-constrained. Figure 1 shows the light curves of AT 2019qiz observed by *Swift* UVOT and ground-based optical facilities including LCO, ZTF, and the Swope telescope at the Las Campanas Observatory. Data reduction with each instrument is detailed in the following subsections.

2.2.1. *ZTF Photometry*

AT 2019qiz was simultaneously observed in the ZTF Mid-Scale Innovations Program field in both g and r bands with a 3-day cadence. The ZTF real-time pipeline performs standard image reduction and subtraction with respect to ZTF template images and distributes the events as alert packets on each observing night (Bellm et al. 2019; Masci et al. 2019). We accessed the pub-

lic alerts of AT 2019qiz via LCO MARS ¹ and used the template-subtracted PSF magnitude to generate the light curves. The last ZTF detection was obtained on Feb 25 2020 in g band as ZTF stopped monitoring the field containing AT 2019qiz. We measured a S/N-weighted offset of $0.13'' \pm 0.17''$ from the ZTF g and r data, confirming that the transient is co-incident with the galaxy nucleus, as expected for a TDE.

2.2.2. Swope Photometry

Optical photometry of AT 2019qiz in $ugri$ was obtained with the 1-meter Swope telescope from 26 Sep 2019 to 1 Mar 2020 with a 2–5-day cadence. The images were reduced using the photpipe imaging and photometry pipeline (Rest et al. 2005, 2014). We subtracted the bias and flattened each frame using bias and sky flat images obtained on the same night and in the same instrumental configuration as each AT 2019qiz image. The images were registered and geometric distortion was removed using 2MASS astrometric standards (Cutri et al. 2003). Using `hotpants` (Becker 2015), we subtracted pre-discovery Pan-STARRS1 (PS1) template images (Flewelling et al. 2016) from each Swope gri frame.

Since we are not yet able to obtain a template image for the u -band, we instead extracted photometry within a $5''$ radius aperture and subtract the host light in the u band by modelling the host galaxy emission. The u band emission of the host galaxy is estimated by fitting the PS1 photometry in $grizy$ bands and the 2MASS photometry in the JHK filters in a $5''$ radius circular aperture with the synthetic stellar population fitting code PROSPECTOR. Our best-fit continuity SFH model with 5 age bins yields a stellar mass of $\log_{10}(M_*/M_\odot) = 10.43 \pm 0.04$ and a metal content of $\log_{10}(Z/Z_\odot) = -1.11^{+0.22}_{-0.45}$, which are consistent with that derived by N20 and van Velzen et al. (2020b).

2.2.3. LCO Photometry

We also obtained optical photometry of AT 2019qiz in ugr bands from Sep 25 2019 to Nov 27 2019 with the Sinistro camera mounted on one of the 1-meter telescopes of the Las Cumbres Observatory (LCO) network in Siding Spring, Australia. Similar to our handling of the Swope photometry, we removed host contamination by performing image subtraction for the g and r band and by modelling the host flux in the same $5''$ aperture for the u band.

2.3. UVOT Photometry

We extracted UV light curves from a series of 42 observations obtained with *Swift* UVOT using a $5''$ circular aperture. The *Swift* target-of-opportunity observations covered the evolution of AT 2019qiz from $\Delta t = -11$ to 168 days. Although the observations were made in all 6 UVOT filters (UVW2, UVM2, UVW1, U , B , and V), we only show the data from the three bluest filters (UVW2, UVM2, and UVW1), where the host galaxy contribution are negligible, in Figure 1. These are also the only *Swift* filters used in our data analysis. The non-detections in the archival GALEX All-Sky Imaging Survey place an upperlimit of $FUV > 20$ mag and $NUV > 20.8$ mag on the host galaxy light. Given that the flux in the *Swift* UV filters is highly dominated by the TDE at the time of the observations, we did not attempt subtracting the host flux from these bands.

2.4. Optical Spectroscopy

We obtained a total of 18 spectroscopic observations with the Kast spectrograph (Miller & Stone 1993) on the Lick Shane telescope, the Goodman spectrograph on the SOAR Telescope (Clemens et al. 2004), and the Low-Resolution Imaging Spectrometer (LRIS) (Oke et al. 1995) on the Keck I telescope. Detailed instrumental configurations are listed in Table 1. We performed 1-D spectrum extraction and flux calibration with standard PyRAF² routines. Observations of standard stars BD+174708 and BD+284211 were used to determine the relative flux calibration and remove telluric features (Foley et al. 2003; Silverman et al. 2012; Dimitriadis et al. 2019). All of the spectra presented in this paper have been corrected for Galactic extinction. We calibrated each spectrum’s absolute flux by comparing the g -band synthetic photometry of each spectrum to the photometry from Swope and LCO imaging data (including host contribution), interpolated to each spectroscopic epoch.

3. ANALYSIS

3.1. Black Hole Mass Estimation

We have not yet been able to obtain high resolution spectroscopy to measure the stellar dispersion of the host galaxy. Nevertheless, N20 has derived a velocity dispersion of $\sigma = 69.7 \pm 2.3 \text{ km s}^{-1}$ from their late-time X-shooter spectrum. Using the scaling relation derived for a sample of low-mass galaxies from Xiao et al. (2011), this velocity dispersion corresponds to a blackhole mass of $\log_{10}(M_{\text{BH}}/M_\odot) = 6.16 \pm 0.43$. Different $M-\sigma$ relations generally agree with an upper limit of

¹ <https://mars.lco.global>

² http://www.stsci.edu/institute/software_hardware/pyraf

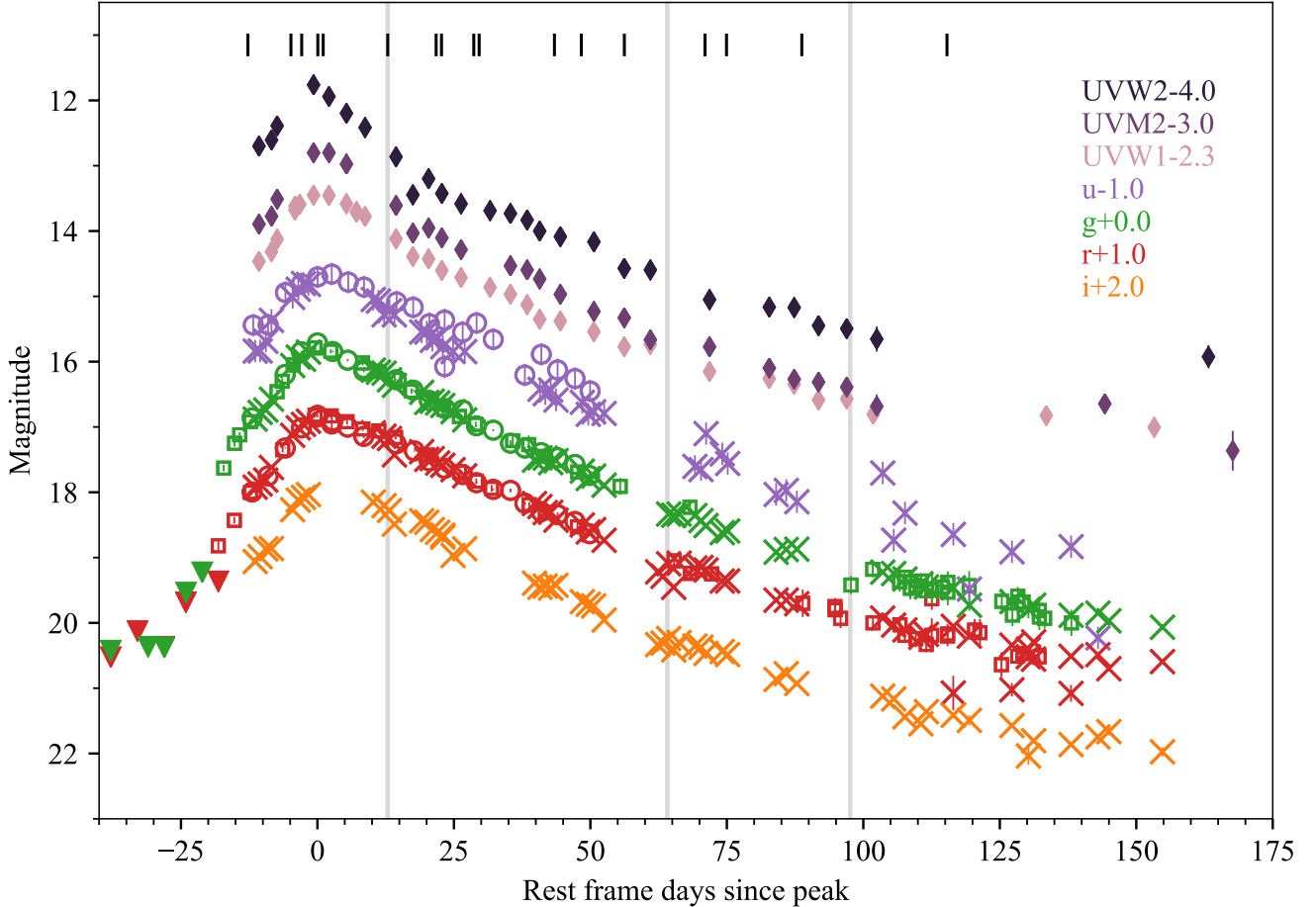


Figure 1. Multi-wavelength light curves of AT 2019qiz. Host contribution have been subtracted from all the optical photometry. Photometry observed with *Swift*, ZTF, LCO, and Swope are marked with diamonds, squares, circles, and crosses, respectively. The triangles mark the upper limits in *g* and *r* filters. The light curves are color-coded by the filters and offset by a constant to aid visualization. Contamination from galaxy light is minimal in the *Swift* UV filters. The *HST* epochs are indicated by the grey vertical lines.

$\log_{10}(M_{\text{BH}}/M_{\odot}) \lesssim 6.5$ (Nicholl et al. 2020). As detailed below, the black hole mass derived from light curve fitting is also consistent with this value. Therefore we use $M_{\text{BH}}=1.4 \times 10^6 M_{\odot}$ when estimating relevant scales throughout the paper.

We also used `MOSFiT` to model the observed UV and optical light curves in Figure 1 in order to derive physical parameters of the TDE, including the black hole mass. The TDE model implemented in `MOSFiT` estimates the bolometric luminosity of the TDE by converting the mass fallback rates from hydrodynamic simulations (Guillochon & Ramirez-Ruiz 2013) with a constant efficiency parameter (Guillochon et al. 2018; Mockler et al. 2019). The program then tries to match the observed flux in each band by reprocessing the bolometric flux with a blackbody photosphere, assuming that the blackbody photosphere evolves as a power law of the mass fallback rate.

The TDE model in `MOSFiT` has 8 parameters, which are listed and defined in Table 1 in Mockler et al. (2019). We present the best-fit values from the `MOSFiT` run for AT 2019qiz in Table 2. The only constraint we imposed on the fitting parameters is for the stellar mass (M_*) to stay below $3M_{\odot}$. This is because M_* is not always well-constrained by `MOSFiT` owing to its degeneracy with the efficiency parameter and it is physically unlikely for M_* to exceed $3M_{\odot}$.

Our derived parameters are generally consistent with that in N20, though the fitting was performed on a different set of optical data. Our results suggest a negligible viscous time, therefore, the fallback time of the most bound debris t_{fallback} approximates the start of the flare. We derived $t_{\text{fallback}} = -25$ days relative to the time of peak light while N20 found $t_{\text{fallback}} = -27$ days. This value is also consistent with that estimated from a photosphere expanding at constant velocity, where

Table 1. Observing details of the optical spectra of AT 2019qiz

| Obs Date | Phase (days) | Telescope + Instrument | Slit Width | Grism/Grating | Exp Time (s) |
|------------|--------------|------------------------|------------|---------------------|---------------------------|
| 2019-09-25 | -13 | Keck + LRIS | 1.0'' | 600/400 + 400/8500 | 450 (blue) 438 (red) |
| 2019-10-03 | -5 | Shane + Kast | 2.0'' | 452/3306 + 300/7500 | 3660 (blue) 3600 (red) |
| 2019-10-05 | -3 | Shane + Kast | 2.0'' | 452/3306 + 300/7500 | 930 (blue) 2×450 (red) |
| 2019-10-08 | 0 | Shane + Kast | 2.0'' | 452/3306 + 300/7500 | 1560 (blue) 1500 (red) |
| 2019-10-09 | 1 | Soar + Goodman | 1.0'' | 400 m2 | 720 |
| 2019-10-21 | 13 | Soar + Goodman | 1.0'' | 400 m2 | 2×720 |
| 2019-10-30 | 22 | Shane + Kast | 2.0'' | 452/3306 + 300/7500 | 1230 (blue) 2×600 (red) |
| 2019-10-31 | 23 | Shane + Kast | 2.0'' | 452/3306 + 300/7500 | 1560 (blue) 1500 (red) |
| 2019-11-06 | 29 | Shane + Kast | 2.0'' | 452/3306 + 300/7500 | 1865 (blue) 3×600 (red) |
| 2019-11-07 | 30 | Shane + Kast | 2.0'' | 300/7500 | 1500 (red) |
| 2019-11-21 | 43 | Shane + Kast | 2.0'' | 300/7500 | 2400 (red) |
| 2019-11-26 | 48 | Keck + LRIS | 1.0'' | 600/400 + 400/8500 | 450 (blue) 438 (red) |
| 2019-12-04 | 56 | Soar + Goodman | 1.0'' | 400 m2 | 1200 |
| 2019-12-19 | 71 | Soar + Goodman | 1.0'' | 400 m2 | 2×1320 |
| 2019-12-23 | 75 | Shane + Kast | 2.0'' | 452/3306 + 300/7500 | 2×1230 (blue) 4x600 (red) |
| 2020-01-06 | 89 | Shane + Kast | 2.0'' | 452/3306 + 300/7500 | 1845 (blue) 3×600 (red) |
| 2020-02-02 | 115 | Shane + Kast | 2.0'' | 452/3306 + 300/7500 | 1230 (blue) 2×600 (red) |
| 2020-09-18 | 340 | Keck + LRIS | 1.0'' | 600/400 + 400/8500 | 910 (blue) 900 (red) |

Table 2. Best-fit parameters from MOSFiT

| Parameter ^a | Value |
|---|-------------------------|
| t_{fallback} (days) ^c | -25^{+1}_{-1} |
| $\log_{10} R_{\text{ph0}}$ | $0.9^{+0.06}_{-0.09}$ |
| $\log_{10} T_{\text{viscous}}$ (days) | $0.61^{+0.12}_{-0.29}$ |
| l_{photo} | $0.66^{+0.03}_{-0.03}$ |
| β | $0.58^{+0.03}_{-0.03}$ |
| $\log_{10} M_{\text{h}} (M_{\odot})$ | $6.14^{+0.09}_{-0.1}$ |
| $\log_{10} \epsilon$ | $-3.47^{+0.13}_{-0.23}$ |
| $M_{*} (M_{\odot})$ | $1.1^{+0.97}_{-0.1}$ |

NOTE—^a See Mockler et al. (2019) for detailed parameter definition.

$\Delta t = -30$ days (see section 3.2). The black hole mass of $\log_{10}(M_{\text{BH}}/M_{\odot}) = 6.14 \pm 0.1$ derived from MOSFiT is in good agreement with that estimated from the $M - \sigma$ relation.

3.2. Blackbody Temperature, Radius, and Bolometric Luminosity Evolution

As a standard TDE analysis procedure, we model the SEDs of AT 2019qiz with a single temperature blackbody. To do so, we first construct the SEDs at epochs with *Swift* observations in all three UV filters

($UVW2$, $UVM2$, and $UVW1$) and interpolate the photometry in the $ugri$ filters measured from ground-based observatories. We show the best-fit blackbody temperature (T_{bb}) and the 10%–90% confidence level in Figure 2. We derive the bolometric luminosity (L_{bol}) at each *Swift* epoch by integrating over the best-fit blackbody spectra and calculate the emitting radius of the blackbody with the Stefan-Boltzmann law, where $L_{bol} = 4\pi R_{bb}^2 \sigma T_{bb}^4$. The evolution of L_{bol} and R_{bb} are also given in Figure 2. Our measurements are in good agreement with that in N20.

The blackbody temperature in AT 2019qiz initially had a constant temperature of $T_{bb} \approx 2.1 \times 10^4$ K as the light curves approached maximum (t_{peak}). From day 0 to day 25, it then started to cool significantly down to $T_{bb} \approx 1.5 \times 10^4$ K. Afterwards, the T_{bb} slowly recovered back to about 1.7×10^4 K and remained roughly constant out to day 100. This initial decline in T_{bb} was also observed in ASASSN-14ae (Holoiien et al. 2014) shortly after discovery around peak light, and in ASASSN-19bt while the light curves were rising (Holoiien et al. 2019b). This cooling phase is short enough to be missed by previous TDE discoveries, where the classification and UV follow-up typically came around or after maximum light hence only the constant temperature phase was observed.

Our derived peak luminosity $L_{\text{peak}} = 6.4 \times 10^{43}$ erg s⁻¹ corresponds to an Eddington ratio of 0.35 assum-

ing a black hole mass of $1.4 \times 10^6 M_\odot$ estimated from the $M - \sigma$ relation. We estimate a total radiated energy of 1.6×10^{50} erg by extrapolating the luminosity linearly out to $t = \pm\infty$. If entirely powered by accretion, this energy would imply an accreted mass of $8.5 \times 10^{-4}(\epsilon/0.1)^{-1} M_\odot$, where ϵ is the accretion efficiency. The small accreted mass compared to the bound stellar mass could imply a low radiative efficiency or a partial disruption, or that we are underestimating the TDE energetics in other wavelengths (e.g. EUV or IR). In fact, we see indications that the best-fit blackbody tends to underestimate the FUV continuum in our *HST* spectra. The luminosity evolution of AT 2019qiz places it in an unoccupied strip on the luminosity-phase plot that is between the “fast and faint” TDE iPTF16fnl and the slower but brighter TDE population (see Fig. 1 in van Velzen et al. (2020a) and Fig. 10 in N20).

The blackbody radius increased monotonically with time toward light curve peak. We estimate an expansion velocity of $2400 \pm 200 \text{ km s}^{-1}$ for the photosphere. It is worth mentioning that the derived photosphere expands at a much slower rate than the BALs ($\gtrsim 10,000 \text{ km s}^{-1}$) in the UV spectra, which either suggests a difference in the physical location of the outflow or that the two kinematic components are unrelated (more discussions in section 4.1). If the photosphere was expanding at this constant velocity during the entire rise, this implies that the most bound debris fell back at $t_0 = -30.7$ days, which is well before the most recent ZTF pre-flare upper-limit at $\Delta t = -21.7$ days. We estimated a similar reference time of -25 days by fitting the luminosity evolution during rise time with a quadratic function $L \propto (t - t_0)^2$. The prediction of a quadratic rise traces back to the “fireball” model that is frequently used to describe SN Ia light curves. The TDE ASASSN-19bt, which has a densely sampled rising light curve by TESS, also exhibits a power-law rise with an exponent ≈ 2 (Holoiien et al. 2019b).

3.3. Evolution of the UV spectra

A sequence of three *HST* UV spectroscopic observations of AT 2019qiz is shown in Figure 3. Among the three *HST* epochs, the spectrum from the first epoch exhibits signatures distinct from that in previous TDEs. The apparent reduction in outflow velocity is also seen in the UV spectra for the first time. Below we describe these differences qualitatively and leave the quantitative details in the following subsections.

In all three epochs, high-ionization broad absorption lines (HiBALs) blueward of the rest wavelengths of N V, Si IV, and C IV can be readily seen. The HiBAL absorption troughs are blueshifted more in the first *HST* epoch

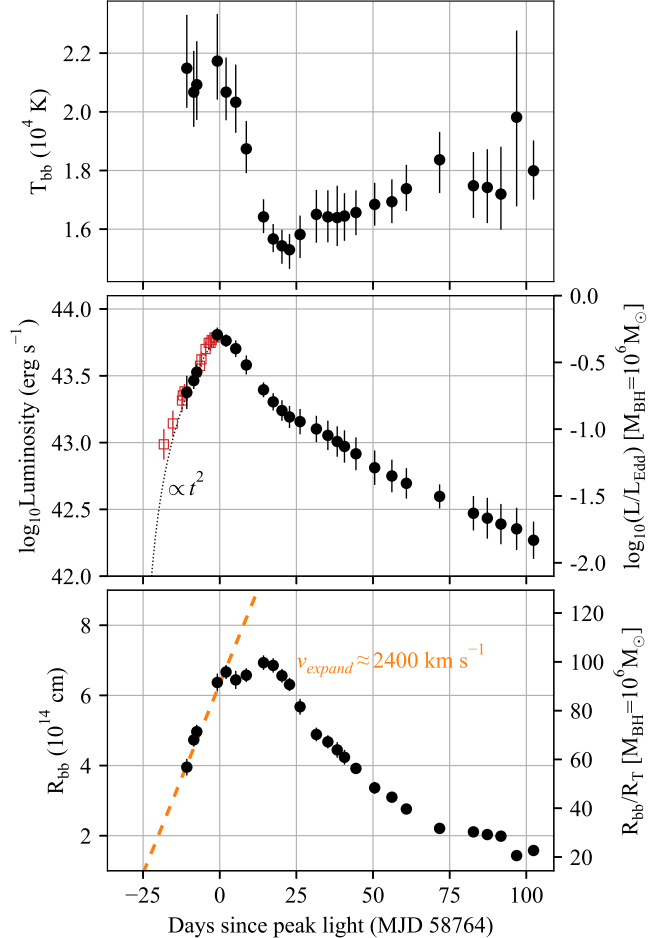


Figure 2. The evolution of blackbody temperature (top), bolometric luminosity (middle), and blackbody radius (bottom) measured from the UV and optical light curves on *Swift* epochs (black circles). We also show the luminosity scaled from *r*-band light curve (open red squares) for the rising part to help visualize the early evolution. The dotted line in the middle panel shows the best-fit quadratic function to the L_{bol} measured from the *Swift* epochs during the rise. The quadratic function asymptotically approaches a reference time $t_0 = -25.3$ days. The dashed orange curve displays the best-fit expansion velocity to the rising part of R_{bb} .

($v \approx 15,000 \text{ km s}^{-1}$ on $\Delta t = 13$ d) and decelerated to $v \approx 10,000 \text{ km s}^{-1}$ in the later two epochs ($\Delta t = 65$ d and 98 d). In addition, the first *HST* spectrum is characterized by broad structures in the NUV ($\lambda_{rest} \gtrsim 1650 \text{ \AA}$). We later identified these broad features to be associated with Al III $\lambda 1857$ and iron (Fe II and Fe III) absorption, making AT 2019qiz the first TDE to be detected with Fe and low-ionization broad absorption lines (FeLoBALs). In fact, we find the BAL pattern in AT 2019qiz sharing more similarities to that in a superluminous supernova (SLSN) than in BAL quasars (BALQSOs), which we discuss in more details in section 3.3.2.

In the first *HST* epoch, we also detect narrow absorption lines with a dispersion of 240 km s^{-1} at the host redshift $z_{abs} \approx z_{gal}$. The narrow absorption lines are only marginally detected in the later *HST* epochs due to lower S/N. However, for the stronger absorption lines in the FUV, their line strengths do not seem to vary significantly between the 1st and 2nd *HST* epochs.

3.3.1. Narrow Absorption Lines

We identified and measured the narrow absorption of both low- and high-ionization lines in the $\Delta t = 13 \text{ d}$ *HST* spectrum and tabulated them in Table 3. To interpret these narrow lines, we model them by defining the “effective continuum”, which consists of the continuum emission and the broad TDE features (emission or absorption) and create a continuum-divided spectrum. This step is done by masking the parts of the spectrum containing narrow absorption lines then smooth and interpolate over the masked wavelengths containing the narrow absorption lines using Gaussian Process with a squared exponential covariance function. We then divided the *HST* spectrum by this effective continuum, leaving only the narrow absorption features. Finally, we modelled these absorption lines with Gaussian profiles and measure their line widths and the equivalent widths (W_r) in the rest-frame. Since the C IV $\lambda\lambda 1548, 1551$ resonance doublet is not resolved in the spectrum, we modelled it by requiring the two components to have the same width. We also fix the width of O I $\lambda 1302$ and Si II $\lambda 1304$ to be the same due to line blending. The smoothed effective continuum, the normalized spectrum, and the best-fit models are shown in Figure 4. From the line fit, we measured a S/N-weighted velocity offset of $70 \pm 90 \text{ km s}^{-1}$ that is consistent with the systemic host velocity using only the isolated and unblended absorption lines. We further place an upper limit of $\lesssim 200 \text{ km s}^{-1}$ on the outflow velocity based on the weak Si II $\lambda 1265$ feature. The average dispersion of the absorption lines is $240 \pm 70 \text{ km s}^{-1}$.

We adopt the multi-ion single-component curve of growth (CoG) analysis to derive the ionic column densities from the measured W_r of the narrow absorption lines assuming that the Doppler broadening parameter b is the same for each ionic species. This assumption holds if all the absorption, regardless of high- or low-ionization lines, all took place in a relatively small region that cannot be resolved by our *HST* spectrum. We solve for b iteratively using the unsaturated, unblended ionic lines with the same lower energy states (Si IV, Fe II UV1, and Mg II). In our best-fit model (Figure 5) $b = 95 \text{ km s}^{-1}$. The column densities for the uncontaminated and unblended ionic species are listed in Table 3.

We note that one caveat of applying the CoG analysis to low-resolution spectrum, such as our STIS observation, is that the derived metal column densities can be underestimated by as much as 1 dex (Prochaska 2006). High quality and high resolution spectroscopy of GRB afterglows suggests that the absorption line structures around strong Fe II lines are characterized by multiple saturated components spreading over a few 100 km s^{-1} . In lower-resolution spectra, these absorption structures may be viewed as a single component with greater effective b . Although the larger b value does not necessarily lead to erroneous inference of the column density, it can sometimes affect the measurements by forcing weaker transitions to be optically thin ($\tau_0 \propto b^{-1}$) even when they are saturated. Fine structures may also be present in the absorption lines in AT 2019qiz. Therefore, we emphasize that the metal column densities displayed in Table 3 should be considered as a lower limit.

3.3.2. Identification of the UV Broad Lines

Before delving into the identification of broad features in AT 2019qiz, we remind the readers that the continuum placement, especially in the FUV, may be quite uncertain. Traditionally, we find that the NUV and optical photometry can be described well by a single temperature blackbody with $T_{bb} \approx \text{a few } \times 10^4 \text{ K}$. This has been confirmed to be generally true by past *HST* observations, where the NUV spectra of most TDEs are characterized by a featureless continuum with a slope that is consistent with the *Swift* photometry in each event (Cenko et al. 2016; Brown et al. 2018; Blagorodnova et al. 2019; Hung et al. 2019). At $\lambda_{rest} < 1600 \text{\AA}$, the common presence of HiBALs often eclipses away a large amount of flux in the FUV continuum and broad emission lines in TDEs, making the FUV continuum placement extra difficult. It is noticed that the FUV continuum can be significantly underestimated by extrapolating the NUV blackbody spectrum, as was found in AT 2018zr (Hung et al. 2019) and also in AT 2019qiz (Figure 3). As such, in the analysis we avoid measuring line properties that are dependent on the continuum (e.g. line flux, balfinity index) except for the narrow absorption lines, where the effective continuum can be determined relatively accurately.

Despite the fact that the blackbody spectrum extrapolated from NUV and optical observations is clearly underestimating the FUV continuum, we keep them in Figure 3 to guide the eye. Broad emission and absorption features are detected in all three epochs. In order to identify the lines, it is natural to compare the *HST* spectra of AT 2019qiz with a BALQSO since both TDE and BALQSO are phenomena driven by accretion and

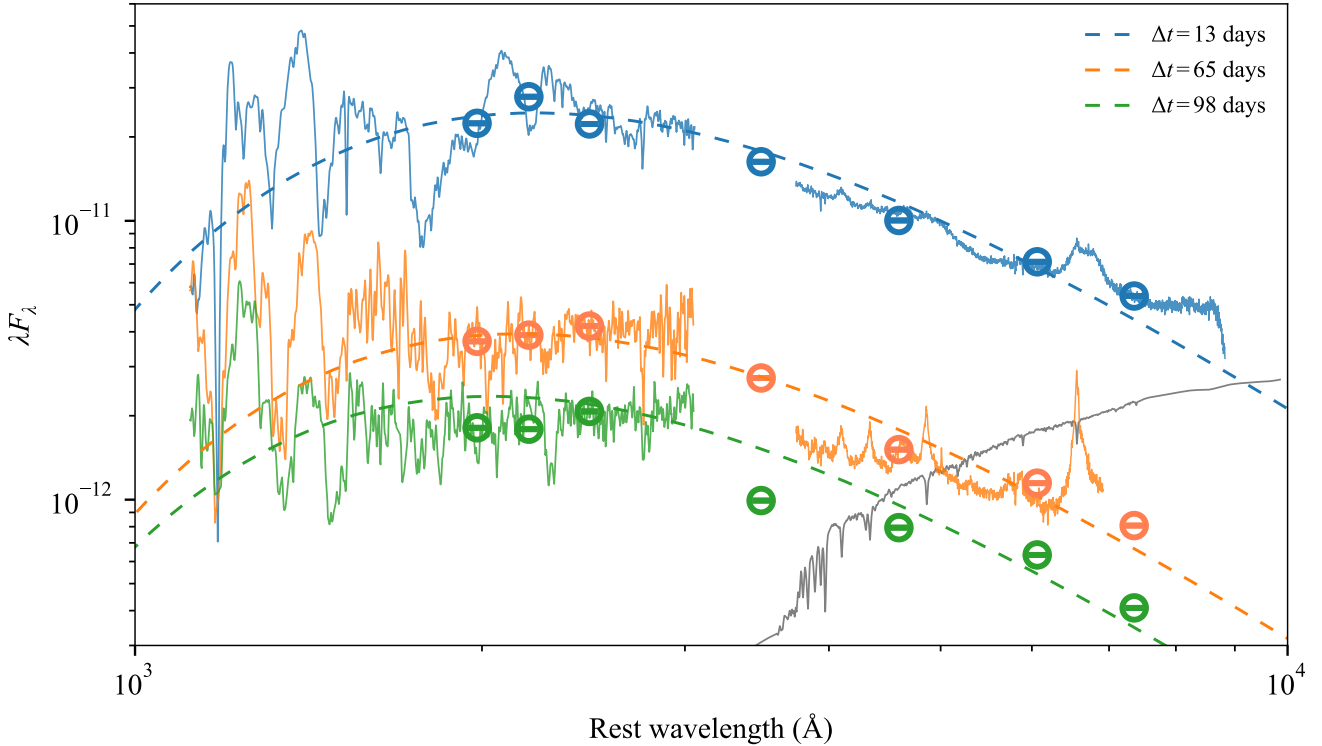


Figure 3. A sequence of *HST* UV spectra of AT 2019qiz, along with the UV and optical ($UVW2, UVM2, UVW1$ and $ugri$) photometry interpolated to the three *HST* epochs. An optical spectrum obtained on $\Delta t = 13$ days (blue) and $\Delta t = 71$ days (orange) are also shown. The dashed lines mark the best-fit single temperature blackbody ($T_{bb} \approx 16,000$ K) to the interpolated UV and optical photometry on each epoch. The grey line shows the best-fit galaxy model from **PROSPECTOR**.

wind. Furthermore, similarities between the rest-frame UV spectra of TDE and BALQSO have been drawn in the past (e.g. Blagorodnova et al. 2019). We find broad structures in both the FUV and NUV sides of the spectrum on day 13. Broad emission lines seem to have formed around the rest wavelengths of high-ionization lines N V, Si IV, and C IV. Blueward of these emission are the absorption troughs associated with these high-ionization transitions. We estimate the blueshift velocity of the broad absorption features (v_w) with respect to the minimum of the troughs. The broad features associated with the Si IV and C IV are blueshifted by $v_w \sim 15,000$ km s $^{-1}$ whereas the velocity offset of the N V absorption trough cannot be precisely measured due to overlap with the geocoronal emission.

In a subclass of BALQSO, the low-ionization broad absorption line (LoBAL) QSOs have UV spectra imprinted by broad absorption of Mg II $\lambda\lambda 2796, 2803$, Al III, and Al II at $\lambda_{rest} > 1750\text{\AA}$. In even rarer cases, absorption of iron lines are present in the QSO spectra and thus these QSOs are termed “FeLoBAL” QSOs. Given the presence of similar ionic species, we compare AT 2019qiz with the spectrum of a SDSS FeLoBAL QSO at $z \sim 2.1$ in Figure 6. From this comparison, we infer

that the absorption around 1800\AA in AT 2019qiz is likely due to a blueshifted ($v_w \sim 9,000$ km s $^{-1}$) Al III $\lambda 1857$ line. At $\lambda_{rest} > 2000\text{\AA}$, the $\Delta t = 13$ d spectrum of AT 2019qiz is characterized by several broad peaks and valleys around the most prominent Fe II and Fe III lines. The iron lines that are possibly associated with the broad NUV features are labelled by dashed lines in Figure 6. If we attribute the absorption features at 2000\AA and 2240\AA to Fe III and Fe II UV2, the measured wavelengths correspond to $v_w \sim 12,000 - 16,000$ km s $^{-1}$, which is in good agreement with that derived from the HiBALs. Unlike the BALQSOs, the HST spectra of AT 2019qiz did not show any significant broad, blueshifted Mg II $\lambda\lambda 2796, 2803$ absorption at any phase (Figure 6).

Intriguingly, we find the $\Delta t = 13$ days UV spectrum of AT 2019qiz to bear more resemblances to the SLSN, Gaia16apd (Yan et al. 2017), than any type of BALQSOs (Figure 6). The similarity between the two spectra possibly stems from the fact that both events had a similar blackbody temperature $T_{bb} \sim 17,000$ K and an expanding photosphere, as probed by the SED fit in section 3.2, during the early phases. The absorption troughs at $1750 < \lambda_{rest} < 2400\text{\AA}$ aligned particu-

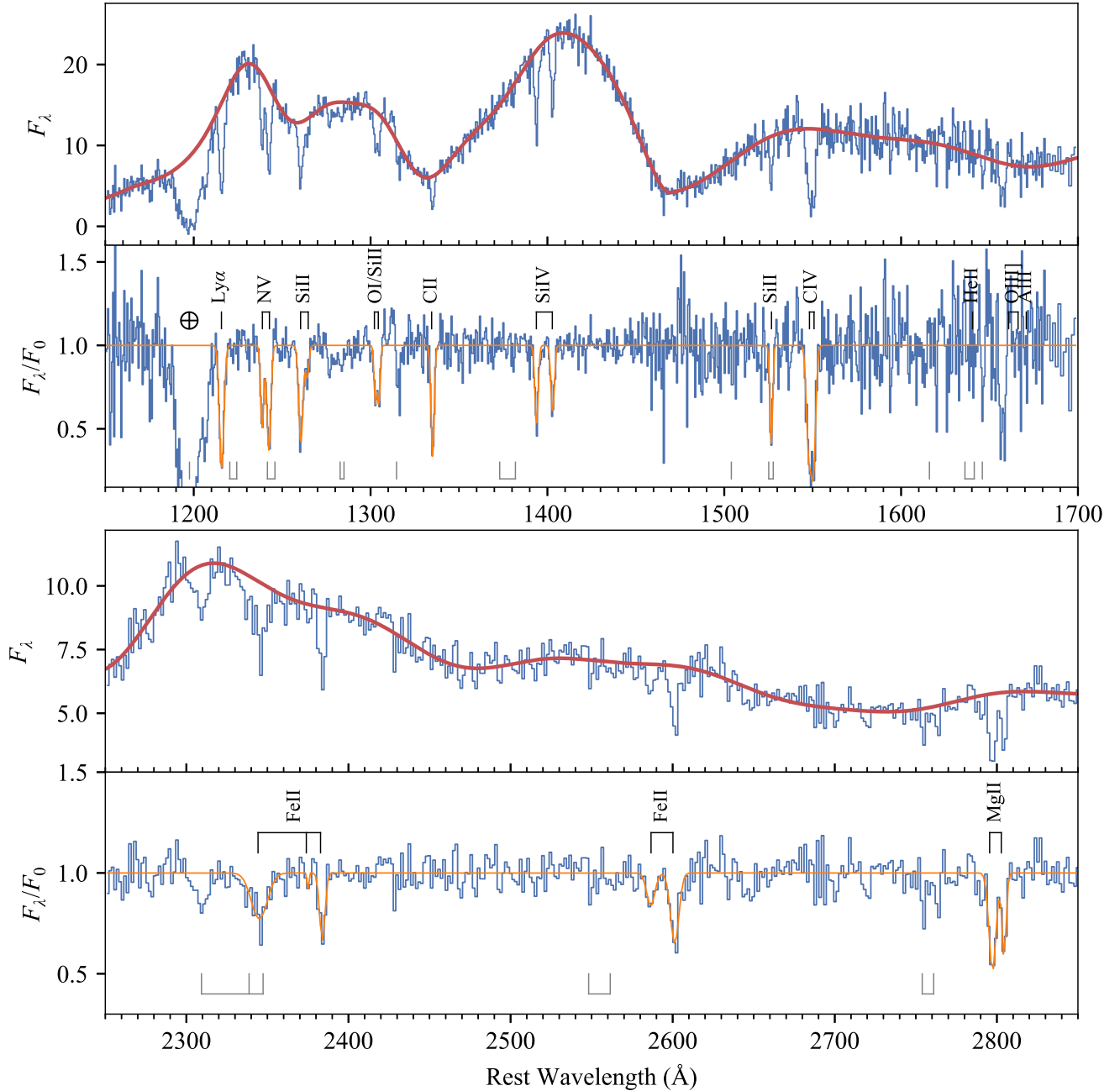


Figure 4. Measurements of the narrow UV absorption lines from the $\Delta t = 13$ days *HST* spectrum. Top panels show the original spectrum (blue) and the smoothed effective continuum (red). The normalized spectrum is shown in the lower panels, where the best-fit Gaussian models are plotted in orange. Green ticks mark the wavelengths of common Galactic absorption lines.

larly well with Gaia16apd after redshifting the SLSN spectrum by $12,000 \text{ km s}^{-1}$. Using the `syn++` model that generates synthetic spectra for homologously expanding atmospheres, Yan et al. (2017) identified the ionic species that contribute to each absorption lines in Gaia16apd. This new comparison makes a difference in the identification of the feature at 1800 \AA

and 2240 \AA . If the ionization state is also similar in AT 2019qiz and Gaia16apd, the 2240 \AA feature would instead be attributed to the absorption of C II with $v_w \approx 11,000 \text{ km s}^{-1}$. In addition, the 1800 \AA feature would not be uniquely associated with Al III, but also with Si II and Ti II. The absorption troughs around the Si IV and C IV lines may also be contributed by other

Table 3. Best-fit parameters of narrow UV absorption line

| Line | λ_0 (Å) | λ_{obs} (Å) | FWHM (Å) | W_r (Å) | z | $\log(gf)$ | $\log N$ (cm $^{-2}$) |
|-------------|--------------------|------------------------|------------------|-------------------|--------|------------|---------------------------|
| Ly α | 1215.67 | 1215.8 | 3.04 ± 0.16 | 2.39 ± 0.15 | 0.0152 | -0.08 | 17.71 |
| N V | 1238.82 | 1238.72 | 2.1 ± 0.21 | 1.13 ± 0.14 | 0.015 | -0.51 | 14.94 |
| N V | 1242.8 | 1242.51 | 2.55 ± 0.19 | 1.72 ± 0.15^a | 0.0149 | -0.81 | ... |
| Si II | 1260.42 | 1260.55 | 2.79 ± 0.25 | 1.74 ± 0.18 | 0.0152 | 0.29 | 15.12 |
| Si II* | 1264.73 | 1264.17 | 2.22 ± 0.66 | 0.45 ± 0.15 | 0.0146 | 0.55 | ... |
| O I | 1302.17 | 1302.72 | 1.72 ± 0.19 | 0.63 ± 0.11^b | 0.0155 | -0.62 | ... |
| Si II | 1304.37 | 1304.72 | 1.72 ± 0.19 | 0.65 ± 0.11^b | 0.0154 | -0.42 | ... |
| C II | 1334.53, 1335.71 | 1335.07 | 2.12 ± 0.14 | 1.53 ± 0.13^b | 0.0155 | -0.62 | ... |
| Si IV | 1393.76 | 1393.83 | 2.23 ± 0.21 | 1.13 ± 0.13 | 0.0152 | 0.03 | 14.29 |
| Si IV | 1402.77 | 1402.94 | 2.3 ± 0.25 | 0.99 ± 0.13 | 0.0152 | -0.28 | 14.29 |
| Si II | 1526.72 | 1526.53 | 1.77 ± 0.15 | 1.12 ± 0.12^a | 0.015 | -0.59 | ... |
| C IV | 1548.20 | 1547.73 | 3.04 ± 0.18 | 1.96 ± 0.20^b | 0.0148 | -0.42 | ... |
| C IV | 1550.77 | 1550.42 | 3.04 ± 0.18 | 2.35 ± 0.20^b | 0.0149 | -0.72 | ... |
| He II | 1640.42 | ... | ... | ... | ... | ... | ... |
| Al II | 1670.79 | ... | ... | ... | ... | ... | ... |
| N III] | 1750.26 | ... | ... | ... | ... | ... | ... |
| C III] | 1908.00 | ... | ... | ... | ... | ... | ... |
| Fe II UV2 | 2344.21 | 2344.99 | 11.77 ± 0.55 | 2.84 ± 0.17^a | 0.0154 | 0.04 | ... |
| Fe II UV2 | 2374.0 | 2374.99 | 0.68 | <0.06 | 0.0155 | -0.55 | ... |
| Fe II UV2 | 2382.77 | 2383.86 | 3.9 ± 0.24 | 1.4 ± 0.11 | 0.0156 | 0.59 | 13.09 |
| Fe II UV1 | 2586.65 | 2586.47 | 5.95 ± 0.61 | 1.04 ± 0.13 | 0.015 | -0.19 | 13.63 |
| Fe II UV1 | 2600.17 | 2601.24 | 6.06 ± 0.28 | 2.27 ± 0.13 | 0.0155 | 0.35 | 13.63 |
| Mg II | 2795.53 | 2797.34 | 5.13 ± 0.19 | 2.67 ± 0.12 | 0.0158 | 0.53 | 13.66 |
| Mg II | 2802.7 | 2804.44 | 3.0 ± 0.17 | 1.35 ± 0.09 | 0.0157 | -0.21 | 13.66 |

NOTE—From the $\Delta t = 13$ days *HST* spectrum. Absorption lines are modelled as individual Gaussian profiles after divided by the local continuum. ^aThe transition may subject to contamination by foreground absorption. ^bBlended with neighbouring lines in the same absorbing system. Therefore we do not use the measured W_r to infer the metal column density.

low-ionization species such as C II and Si II. While many LoBALs are detected in the day 13 UV spectrum, the lack of Mg II $\lambda\lambda 2796, 2803$ in AT 2019qiz would possibly need to be explained by the composition.

The broad UV features evolved significantly from day 13 to day 65. The most remarkable difference is that the absorption troughs associated with the high ionization Si IV and C IV $\lambda\lambda 1548, 1551$ lines became redder, decelerating from $v_w \approx 15,000$ km s $^{-1}$ to $v_w \approx 10,000$ km s $^{-1}$ (Figure 7). It is also noticed that the NUV spectrum became featureless and UV spectra resemble that of previously observed TDEs more at later epochs. The spectra of day 65 and day 98 are very similar except that the bluest Si IV absorption edge seems to have moved to a slightly lower velocity on day 98 (Figure 7).

3.4. Optical Spectroscopic Analysis

We show a sequence of 18 optical spectra of AT 2019qiz in Figure 8. The spectroscopic features in AT 2019qiz underwent significant changes on a timescale of days to weeks. This is best illustrated by the evolution in the shape of the H α emission (Figure 9). The pre-peak and early post-peak spectra from day -13 to day 13 are characterized by a blue continuum with very broad emission features around H α and He II $\lambda 4686$. The latter is likely contaminated by the emission from H β as the entire broad feature runs from rest wavelength 4400–5200Å. During this stage, the H α emission structure spans a FWHM of 2.6×10^4 km s $^{-1}$. We fit this broad H α feature with a double Gaussian function and derived two components with similar FWHMs of $\sim 1.5 \times 10^4$ km s $^{-1}$ centered roughly at the rest wavelength of H α and at a

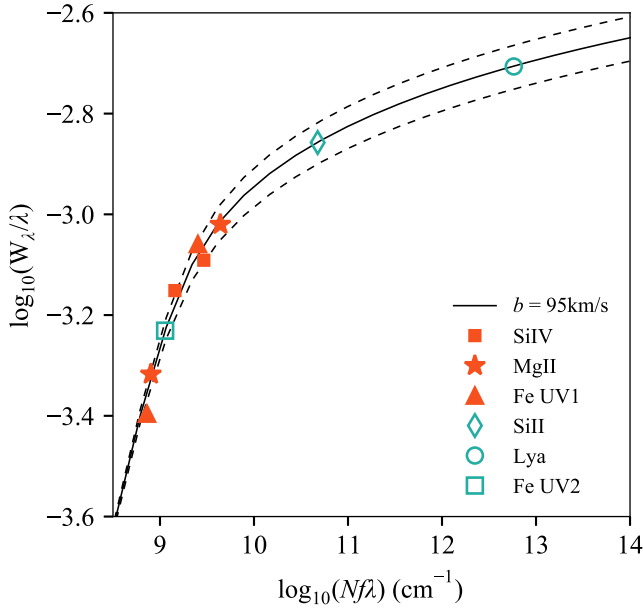


Figure 5. The best-fit CoG curve with $b = 95 \text{ km s}^{-1}$ is shown by the black solid curve. The dashed curves mark the $\pm 10 \text{ km s}^{-1}$ uncertainty in b . Unblended transitions with multiple components used to constrain the fit are marked by red solid symbols. We interpolate the ionic column density for spectral lines with only a single measured component (green open symbols) to the best-fit curve.

redshift of $1.6 \times 10^4 \text{ km s}^{-1}$. The red component has a weaker line flux that is about half of that of the blue component.

On day 22, the $\text{H}\alpha$ emission line profile changed dramatically, with a narrow component appearing around the rest frame $\text{H}\alpha$ wavelength. We then model the $\text{H}\alpha$ emission with three Gaussians simultaneously while requiring the narrow component to have a $\text{FWHM} < 6000 \text{ km s}^{-1}$. The best-fit model consists of a broad $\text{H}\alpha$ base, which is the sum of two Gaussians as in the earlier epochs, with a FWHM of $2.1 \times 10^4 \text{ km s}^{-1}$ and a narrow $\text{H}\alpha$ component with a FWHM of $3,000 \text{ km s}^{-1}$ centered at zero-velocity. During this time, the blue and red component of the broad $\text{H}\alpha$ emission became almost equally strong while the velocity offset of the red component decreased to $1.1 \times 10^4 \text{ km s}^{-1}$.

The broad $\text{H}\alpha$ base continues to decay while the narrow $\text{H}\alpha$ remains strong in all later epochs. The broad $\text{H}\alpha$ has not only showed a decrease in line flux but also a change in the line shape. From day 71 onward, the broad $\text{H}\alpha$ shifted to a single Gaussian centered around the rest $\text{H}\alpha$ wavelength where the red shoulder detected with $v > 10,000 \text{ km s}^{-1}$ in previous epochs disappeared. The FWHM of the broad $\text{H}\alpha$ dropped to $\sim 12,000 \text{ km s}^{-1}$. The FWHM of the narrow $\text{H}\alpha$ emission fluctuates be-

tween $3,000$ and $4,000 \text{ km s}^{-1}$ since it first appeared around day 22.

Narrow Balmer emission lines from higher excited states and narrow Bowen emission ($\text{He II} + \text{N III}$) likely also appeared from day 22 onward. However, it is only after day 49 have the broad emission and continuum faded enough for the narrow lines to be detected. The presence of both the Balmer lines and $\text{He II} + \text{N III}$ makes AT 2019qiz a TDE-Bowen, which is a spectral class that makes up about half of the optical TDE population defined in [van Velzen et al. \(2020b\)](#). On day 71 when the narrow emission lines are the strongest, we measured a FWHM of $4,000 \text{ km s}^{-1}$ for $\text{H}\beta$ and a FWHM of $3,100 \text{ km s}^{-1}$ for $\text{H}\gamma$. The line ratio $\text{H}\alpha/\text{H}\beta \sim 1.2$ corresponds to a flat Balmer decrement, which has also been reported in several TDEs (e.g. AT 2018hyz; [Hung et al. 2020](#); [Short et al. 2020](#)). We also measured a $\text{H}\gamma/\text{H}\beta \sim 0.6$ and a $\text{He II} + \text{N III}$ to $\text{H}\beta$ line ratio of ≈ 1 .

3.5. Host galaxy and the X-ray emission

The host galaxy of AT 2019qiz is 2MASX J04463790–1013349 (WISEA J044637.88–101334.9) at $z = 0.0151$. The r -band Pan-STARRS image reveals that the host galaxy is a spiral galaxy with a clear bar structure. [N20](#) measured a Sersic index in the range of $5.2 – 6.3$, which is considered high compared to the galaxy sample in the same blackhole mass bin ([Law-Smith et al. 2017](#)). Like many other TDE host galaxies, AT 2019qiz also situates in a galaxy with a more concentrated star population ([French et al. 2020](#)).

In the late-time optical spectra of AT 2019qiz, we detect nebular emission lines $[\text{O III}]\lambda\lambda 4959, 5007$ and $[\text{N II}]\lambda\lambda 6548, 6583$ that are indicative of pre-flare AGN activity. Given that the TDE light has faded substantially in the $\Delta t = 340$ days spectrum, we fit its stellar and gas kinematics simultaneously using the Penalized PiXel-Fitting (pPXF) package ([Cappellari 2017](#)) with the MILES stellar library ([Figure 10](#)). In addition to the narrow nebular emission lines, we added a second gas component in our fit to account for the TDE Balmer emission at late time, which has also been observed in previous TDEs (e.g. AT2018zr [Hung et al. 2019](#)). Our best-fit width for the TDE Balmer lines ($\text{FWHM} \approx 2,000 \text{ km s}^{-1}$) is consistent with the width of the narrow $\text{H}\alpha$ component in earlier TDE spectra ($22 \leq \Delta t \leq 115$ days). We measured the flux of the host emission lines and plot the line ratios in a BPT diagram ([Figure 10](#)). The line ratios are in good agreement with the nebular emission lines being produced by AGN photoionization.

During the flare, [N20](#) measured a weak X-ray luminosity of $L_X = 5.1 \times 10^{40} \text{ erg s}^{-1}$ in AT 2019qiz that

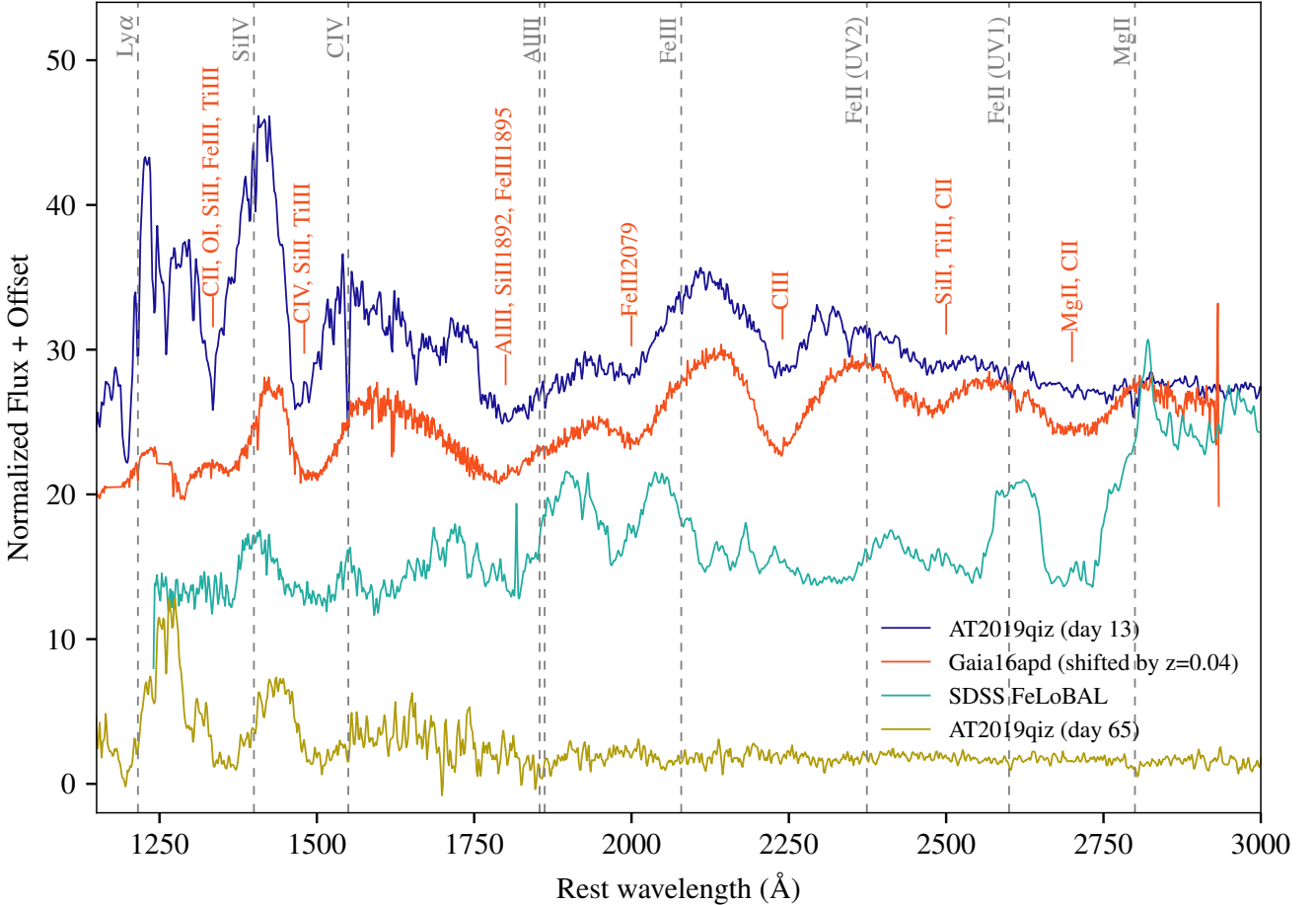


Figure 6. UV spectra of AT 2019qiz on day 13 and day 65, compared to Gaia16apd (Superluminous Supernova Yan et al. 2017), and SDSS J090152.04+624342.6 (FeLoBAL QSO Wang et al. 2017). The first UV spectrum of AT 2019qiz bears a stronger resemblance to that of Gaia16apd. The orange labels mark the potential contributing species identified in Yan et al. (2017).

is 2–3 orders of magnitude below the UV and optical luminosity. N20 associated the X-ray emission with the TDE rather than the AGN due to variability in the X-ray flux and the evolution of the hardness ratio. However, the hardness ratio of -0.1 ± 0.04 from the merged XRT observations is on the higher end of the TDE distribution when compared to X-ray bright TDEs such as ASASSN-14li, and is more similar to those seen in AGNs (Auchettl et al. 2018). Therefore, the possibility of an AGN-driven X-ray emission in AT 2019qiz cannot be completely ruled out.

4. DISCUSSION

4.1. Photosphere evolution

The UV and optical photometry reveals the evolution of the blackbody radius from the pre-peak phase out to $\Delta t \sim 100$ days. The blackbody radius was initially expanding linearly at a velocity of $2,400 \text{ km s}^{-1}$ up to the time of peak light in the UV and optical. The con-

stant velocity phase is then followed by a constant radius phase for ~ 25 days before it began to shrink with time like those observed in previous TDEs, as a result of the combination of decreasing luminosity and constant color temperature.

Our intensive follow-up of the optical photosphere and the BALs in the UV spectra strongly support the presence of an outflow that evolved significantly with time in AT 2019qiz. Various models have been proposed to explain the origin of TDE outflows (Strubbe & Quataert 2009; Lodato & Rossi 2011; Dai et al. 2018; Lu & Bonnerot 2020). In such models, the wind typically has a non-spherical configuration, and the velocity can have some variation depending on the wind launching radius and observer inclination. However, when strong optical emission is observed, one can assume that the wind is mass-loaded and optically thick along the line of sight, thus justifying the adoption of a quasi-spherical model for studying the wind physics

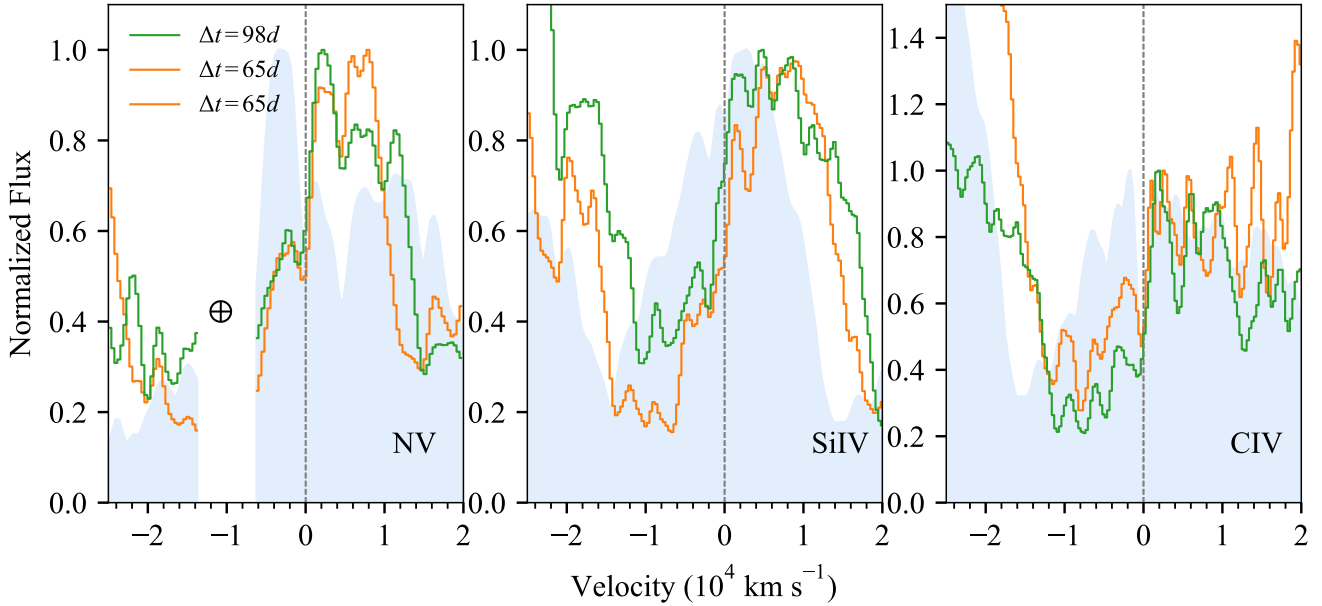


Figure 7. Three epochs of HST STIS spectra in velocity space with respect to the rest-wavelength of high ionization lines: N V, Si IV, and C IV. The region affected by geocoronal airglow emission indicated by a circled plus symbol is truncated. The UV spectrum from the first HST epoch is shaded in pale blue while the spectra from the second and the third epochs are plotted as orange and green curves, respectively. It can be seen that the absorption troughs shifted to lower velocities as time progressed from 13d to 65d, which makes the emission lines seem more redshifted.

(Metzger & Stone 2016; Roth et al. 2016). Here we construct a simple 1-D wind model, where the mass outflow rate $\dot{M}_{\text{wind}} = 4\pi r^2 \rho_{\text{wind}} v_{\text{wind}}$, based on the observed results. The photospheric radius (R_{ph}) corresponds to the surface of electron scattering where the optical depth $\tau_e \propto \rho(r = R_{\text{ph}}) R_{\text{ph}} = 2/3$. Therefore, R_{ph} should be proportional to the mass outflow rate divided by the wind velocity $R_{\text{ph}} \propto \dot{M}_{\text{wind}}/v_{\text{wind}}$. If we assume that the observed luminosity scales roughly linearly with the accretion rate \dot{M}_{acc} , then from the three UV BAL velocity measurement at $\Delta t = 13, 65$, and 98 days post peak, we can derive a scaling relation $v_{\text{wind}} \propto \dot{M}_{\text{acc}}^{0.2}$. Putting this together with the observed photosphere radius evolution $R_{\text{bb}} \propto \dot{M}_{\text{acc}}^{0.6}$ during these times, we can constrain that $\dot{M}_{\text{wind}} \propto \dot{M}_{\text{acc}}^{0.8}$. This is consistent with the results in Strubbe & Quataert (2009); Lodato & Rossi (2011) stating that a stronger wind is launched at earlier phases in TDEs when the mass fallback rate is higher.

In the analytical model developed by Metzger & Stone (2016), only a small fraction of the bound debris accretes onto the black hole. The binding energy of the accreted mass naturally gives rise to a quasi-spherical outflow that is massive enough to absorb and reprocess the hard EUV/X-ray photons into UV and optical emission. One prediction of the Metzger & Stone (2016) model is that the TDE light curve can deviate from the mass fallback rate ($\propto t^{-5/3}$) at early times due

to photon trapping. They find that the observed luminosity can be suppressed at first due to adiabatic losses in the inner wind, resulting in a flatter light curve than $\propto t^{-5/3}$. The suppression continues until the trapped photons are advected to a radius where photon diffusion time is short compared to the outflow expansion time on a timescale of $t_{\text{tr}}/t_{\text{fallback}} \approx 2.6\beta^{3/5} M_{bh}^{-1/2} m_{\star}^{1/5} R_{in,6}^{-3/5}$. At this point, photons can diffuse out of the ejecta freely and thus allowing the photosphere to cool. The effect of photon trapping aligns with the observed T_{bb} evolution in AT 2019qiz, where the measured temperature started to decrease at around one fallback time. This may also explain why the cooling in ASASSN-14ae and ASASSN-19bt occurred at different phases, since the trapping time is dependent on other parameters.

The balance between a decreasing luminosity and temperature cooling gives rise to the plateau in the blackbody radius from $\Delta t = 0$ to 25 days. In practice, the photosphere velocity does not need to follow the outflow velocity if the density or ionization of the photosphere are changing. That is, even if the gas that is producing the UV and optical continuum continues expanding at a constant velocity, a reduction in the electron density can move the electron scattering photosphere inward, and leads to a plateau or even a decrease in the derived blackbody radius as observed in AT 2019qiz.

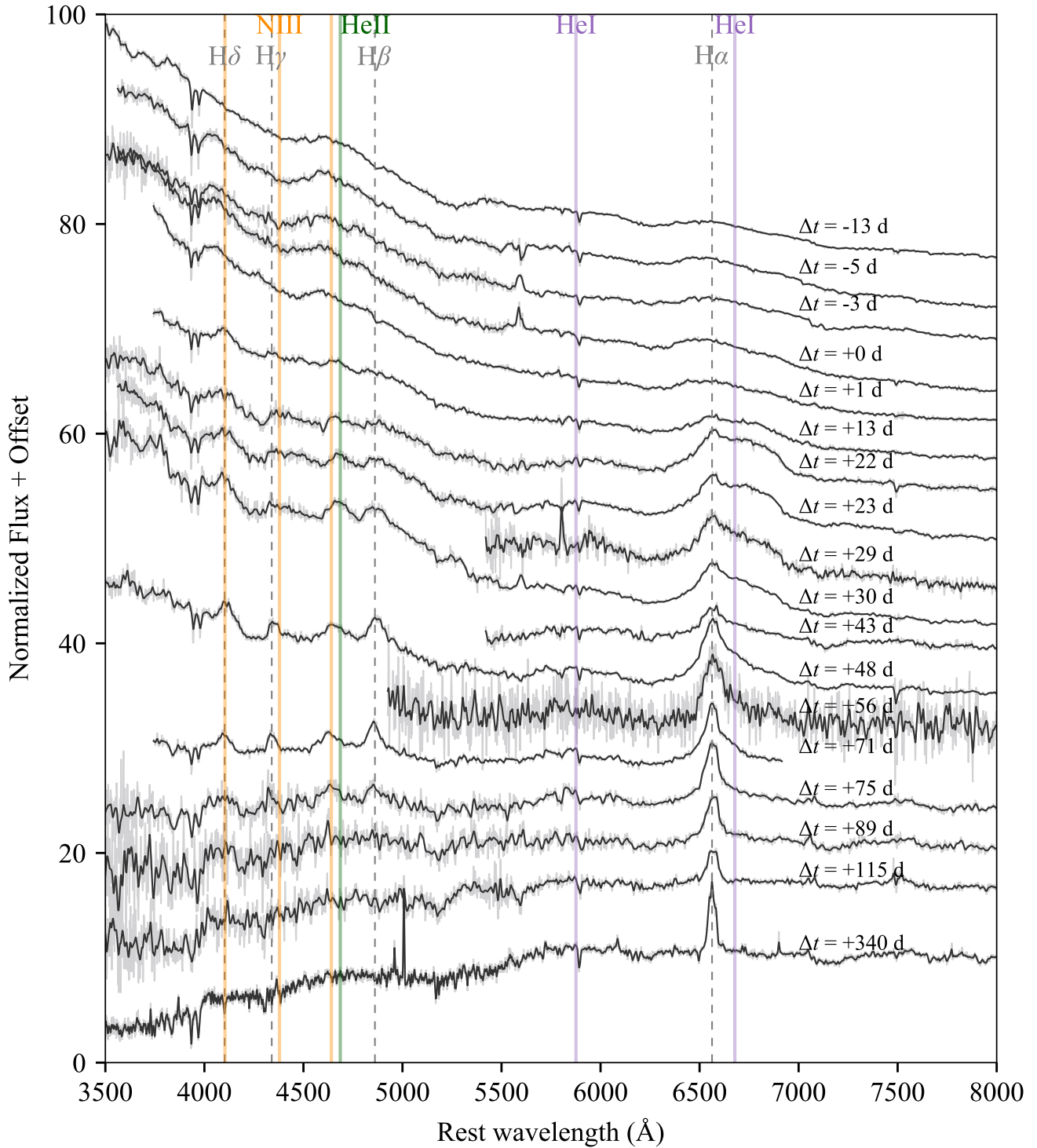


Figure 8. Optical spectra of AT 2019qiz obtained between $\Delta t = -13$ days and $\Delta t = 340$ days. The grey dashed lines mark the wavelengths of the Balmer series. Coloured vertical lines mark the wavelengths of N III (orange), He II (green), and He I (purple). Significant line profile evolution is seen toward the H α emission.

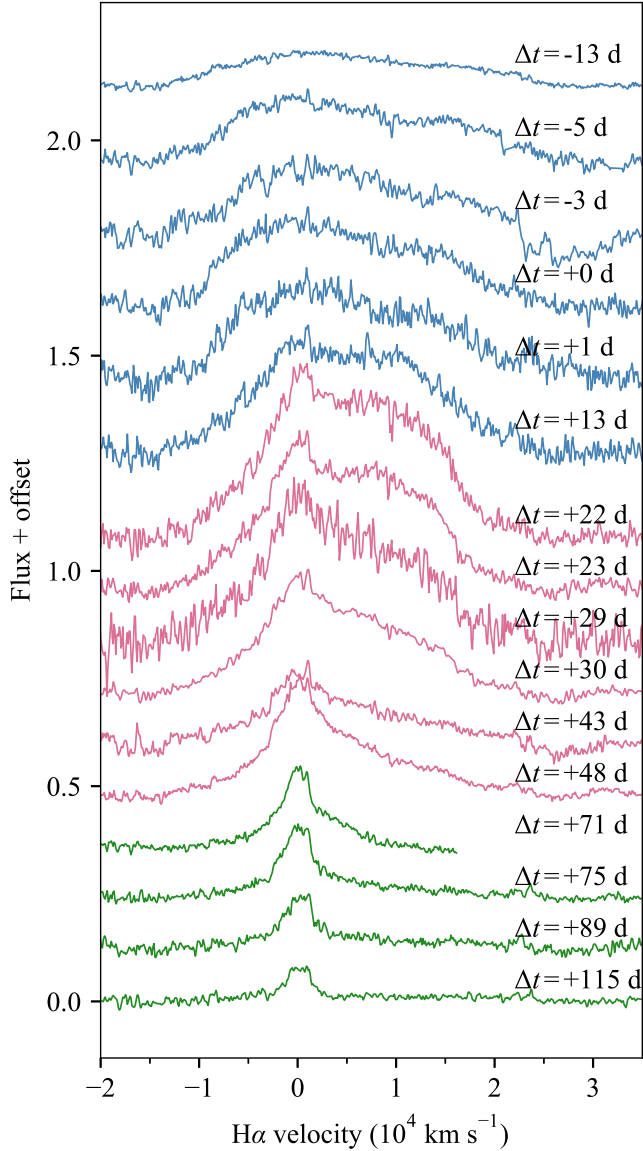


Figure 9. Evolution of the H α emission profile after continuum subtraction. We used models with a different number of Gaussian components to fit the line at different phases. The H α line profile in the earliest spectra can be characterized by two broad Gaussians (blue). In the post-peak period, a narrow component became apparent, which motivated us to adopt a three component model (pink) to describe the line shape. In later spectra, the red shoulder in the broad H α disappeared, thus we use a narrow and a broad component centered around the H α to model the emission line (green).

4.2. TDE UV spectra

Blueshifted broad absorption features detected in AT 2019qiz signify the presence of outflowing gas at a phase as early as $\Delta t = 13$ days. The ejecta producing the BALs would have reached a distance of $\sim 5 \times 10^{15}$ cm if it has been moving at the same ve-

locity since the most bound debris returned to the pericenter (assuming $t_{\text{fallback}} = -25$ to -30 days). BALs have also been detected at different stages in almost all of the TDEs observed with UV spectroscopy, including PS1-11af, iPTF15af, iPTF16fnl, and AT2018zr (Chornock et al. 2014; Blagorodnova et al. 2019; Brown et al. 2018; Hung et al. 2019). Among the HST TDE sample, ASASSN-14li is the only object that exhibits pure broad emission lines (Cenko et al. 2016).

To this date, iPTF16fnl ($\Delta t = 7, 22, 44$ days), AT 2018zr ($\Delta t = 23, 36, 41, 59, 62$ days), and AT 2019qiz ($\Delta t = 13, 65, 98$ days) are the only TDEs with a sequence of HST UV spectroscopic observations (Brown et al. 2018; Hung et al. 2019). Among these, AT 2019qiz has the longest observational baseline. Each of these TDEs undergoes a very different evolution path. In the earliest HST epoch, iPTF16fnl was observed with weak HiBALs (FWHM $\sim 6,000$ km s $^{-1}$) that diminished over time. AT2018zr started resembling ASASSN-14li with a UV spectrum characterized by broad emission lines. Broad absorption troughs blueward of both high- and low-ionization species with a velocity offset of $\sim 0.05c$ started to appear from day 59 onward. AT 2019qiz exhibits a rare FeLoBAL spectrum in the first epoch, which then transitioned into a HiBAL spectrum at later two epochs. The HiBALs remained strong in AT 2019qiz though the outflow velocity decreased from 15,000 to 10,000 km s $^{-1}$ in ≈ 50 days (Figure 7). The decrease in outflow velocity is consistent with the theoretical prediction, where the wind becomes weaker with time as the mass fallback/accretion rate declines.

We select the most representative phases from the multi-epoch HST spectra for iPTF16fnl, AT2018zr, and AT2019 qiz and compare them with the single epoch spectra obtained for all the rest TDEs in Figure 11. While we arrange the spectra in Figure 11 with respect to phase, we find that any two spectra obtained at a similar phase do not guarantee similarity.

The spectrum that stands out in the current UV TDE population is the AT 2019qiz UV spectrum on $\Delta t = 13$ days Figure 11. The presence of FeLoBALs in the UV spectrum of AT 2019qiz is in accordance with the reprocessing scenario. Photoionization models of FeLoBAL QSOs, which are typically X-ray faint, suggest that high column densities are required in order to produce the iron features (e.g. $N_H \sim 10^{20.6}$ cm $^{-2}$ Korista et al. 2008). Analogously, the BAL clouds need to be shielded from the hard X-ray photons to form the FeLoBAL in AT 2019qiz. The shielding gas may be an inner wind made up by material that has fallen back more recently as proposed in the Metzger & Stone (2016) model. In a few fallback time, the column density drops low enough

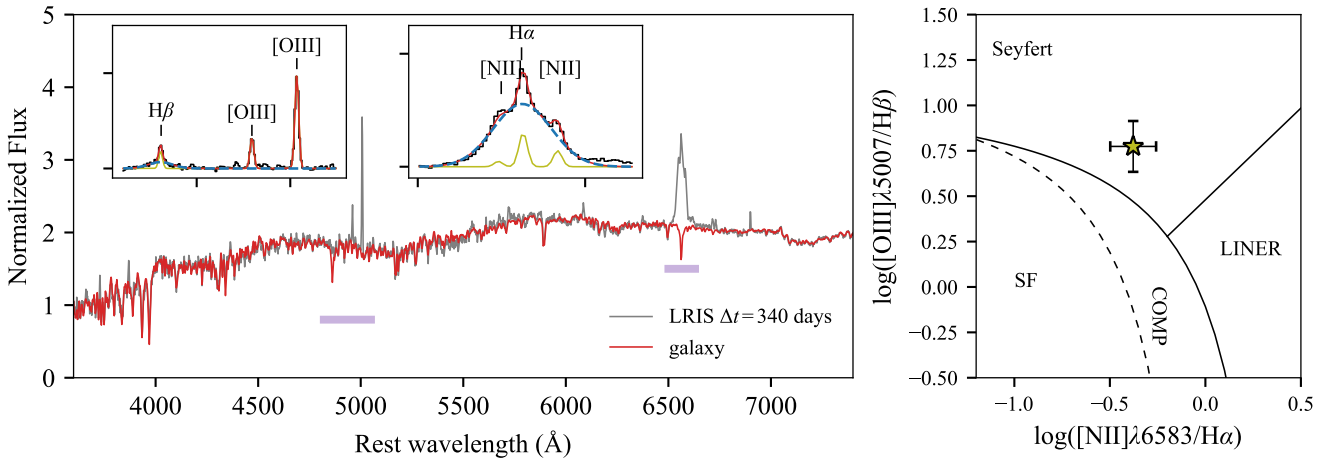


Figure 10. Left: Late-time Keck spectrum of AT 2019qiz (grey) overlaid with the best-fit host galaxy model (red) with pPXF. We fit the stellar population as well as the host and TDE emission lines simultaneously. The emission line spectrum (host-subtracted) around $\text{H}\alpha$ and $\text{H}\beta$ are shown in the insets, where the TDE emission is marked by blue dashed lines and the host emission is plotted in yellow. Right: The emission line diagnostic diagram. The narrow line ratios of the host galaxy of AT 2019qiz falls in the region occupied by AGNs.

such that the ejecta become transparent to the X-ray and EUV photons. This likely explains why the iron and low-ionization features disappeared, leaving only the Hi-BALs in later *HST* spectra of AT 2019qiz.

As shown in Figure 6, this spectrum is more like that observed in SLSN instead of in TDEs or BALQSOs. According to the Metzger & Stone (2016) model, the outflow properties of TDEs may be similar to that in engine-driven supernovae as black hole accretion continues to inject energy into the ejecta. The observed similarities between the early-time UV spectral features in AT 2019qiz and that in the SLSN Gaia16apd are strong evidence supporting this connection.

The HiBAL TDE spectra, which are seen in at least half of the TDEs at a later phase, all seem to be very similar except for small differences in outflow velocities ($6,000 - 15,000 \text{ km s}^{-1}$). The reduction in the mass fallback rate and the expanding ejecta likely facilitated changes in the ionization structure and the column densities that cause the UV spectral features to transition from SLSN-like to more BALQSO-like. It is worth noting that the CIV and SiIV emission always appear to be weaker than the NV emission in TDEs than that in AGNs and BALQSOs. This may be attributed to the stellar debris having a higher N/C ratio due to CNO processing in the stellar core (Kochanek 2016; Cenko et al. 2016; Yang et al. 2017; Law-Smith et al. 2020).

The diverse properties of the TDE UV spectra perhaps reflect the intricate processes involved in a TDE such as accretion disk formation and wind launching. In recent theoretical developments, studies have shown that orientation effects can, at least in part, explain the

diverse broadband and line emission/absorption properties seen in TDEs (Dai et al. 2018; Parkinson et al. 2020).

Parkinson et al. (2020) simulated spectra with broad emission lines (BELs) and BALs with a disk and wind model for TDEs. In particular, they rendered spectra that consist of purely broad emission lines (BELs) at sightlines that do not intersect the disk wind. While viewing angle may be responsible for the dichotomy of BELs and BALs in TDE spectra, it does not explain how one object can transition from BEL to BAL, as seen in AT 2018zr during the first 60 days (Hung et al. 2019). The SLSN-like early spectrum of AT 2019qiz further calls for a time-dependent, multi-zone wind model to be considered in future TDE simulations. Including AT 2019qiz, the high occurrence of BALs in TDE spectra (c.f. QSO) continues to support a wide-angle wind geometry in TDEs (Hung et al. 2019; Parkinson et al. 2020).

4.3. Origins of the multi-component $\text{H}\alpha$ emission

The accretion disk, outflow, and the bound stellar debris are all possible production sites of $\text{H}\alpha$ emission in a TDE. In a glimpse, the broad $\text{H}\alpha$ component in AT 2019qiz may be reminiscent of a disk line profile with an intermediate inclination angle (i) such that the peaks corresponding to materials moving away and toward the observer are not resolved (e.g. Holoi et al. 2019a; Liu et al. 2017). If due to rotation, the measured separation of $\sim 15,000 \text{ km s}^{-1}$ between the two fitted peaks in the pre-peak epochs implies a disk size of $400(\frac{\sin i}{0.5})^2 R_g$. However, the fast evolution of this

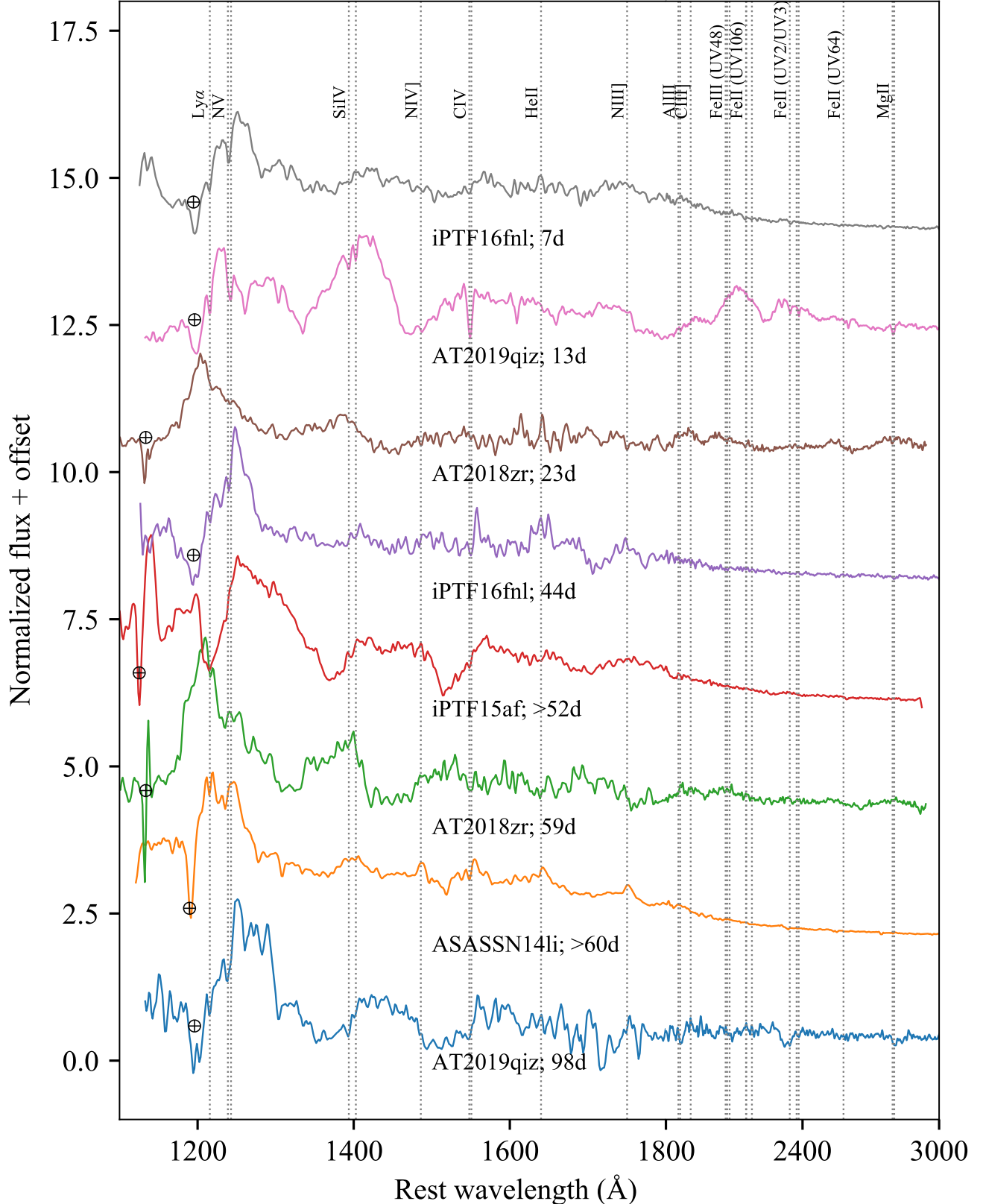


Figure 11. All TDE spectra have been normalized to rest wavelength 1700Å. Note that the scale on the x-axis has been compressed for the NUV segment (1800–3000 Å) to allow more detailed examination of the FUV portion of the spectra.

broad component, with FWHM shrinking by as much as $\approx 50\%$ in roughly 80 days, is hard to reconcile with the disk origin since changes in the disk geometry are expected to occur on longer timescales. In the double-peaked TDE AT 2018hyz, the H α line widths remained roughly constant for at least a duration of 100 days (Figure 12; Hung et al. 2020).

The width of the broad Balmer emission in TDEs is typically on the order of 10^4 km s $^{-1}$. This value is comparable to the expected outflow velocity (e.g. Strubbe & Quataert 2009; Metzger & Stone 2016) in a TDE and therefore hints on the association. Roth & Kasen (2018) first proposed that asymmetric emission lines may result from an optically thick, outflowing gas that is expected to be common in TDEs. The resulting line lacks the blueshifted absorption portion of a P-Cygni line profile when the excitation temperature of the line is higher than the brightness temperature of the photosphere. Indeed, more and more TDEs are found to have emission line shapes deviating from a simple Gaussian (e.g. ASASSN-14ae, AT2018 zr, AT2018 hyz...etc). Hung et al. (2019) found a good fit to the flat-topped H α emission in AT2018 zr with this model, though an elliptical disk within a certain parameter space also produces such line shape (Holczer et al. 2019a). N20 explored this possibility by comparing the Roth & Kasen (2018) model with the spectra of AT 2019qiz. In summary, N20 found the model with an outflow velocity of 5,000 km s $^{-1}$ to be the best match to the H α line profile in earlier and later epochs in AT 2019qiz. However, in the epochs where the H α emission is the strongest, the Roth & Kasen (2018) model fails to replicate the strong red wing of the line profile. The discrepancy may be resolved by adopting a higher opacity, changing the photosphere radius, or allowing for asymmetries in the outflow.

The potential correlation between the HST UV spectral features and the broad H α component in AT 2019qiz could lend further support to the outflow origin of the broad H α emission. We observed a reduction in the velocity of both the HiBALs in the UV and in the broad H α component in the optical (Figure 12). The optical spectra with a higher cadence than the HST UV follow-up find the FWHM to decrease from $\sim 22,000$ km s $^{-1}$ on $\Delta t = 13$ days to $\lesssim 15,000$ km s $^{-1}$ on $\Delta t \geq 48$ days. This change is well-reflected in the $\Delta t = 65$ days HST spectra, which decelerated by $\sim 5,000$ km s $^{-1}$ since the first HST observation on $\Delta t = 13$ days.

4.4. Origin of the Narrow UV Absorption Lines

As mentioned, we are unable to constrain the variability in the narrow absorption lines confidently due to lower S/N in the later HST epochs. However, the FUV

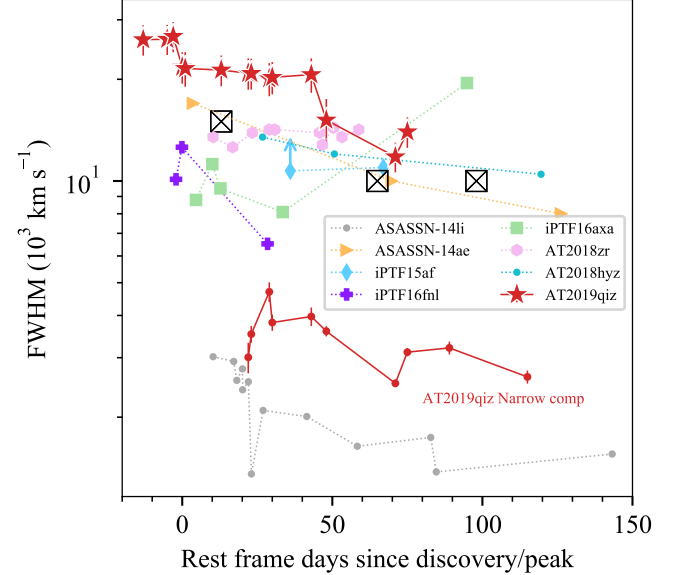


Figure 12. The evolution of H α FWHM with other TDEs. The FWHM of the broad H α component is shown with red stars while the FWHM of the narrow H α component is shown with red circles. Crossed boxes mark the BAL velocity at three *HST* epochs. It can be seen that the timing of the decrease in the broad H α width is consistent with the change in outflow speed probed by the BALs.

spectrum from the 2nd HST epoch does have sufficient S/N to reveal stronger absorption lines with $W_r \gtrsim 1.0$. We find these lines to have a comparable strength in the day 13 and day 65 spectra.

GRB afterglow spectra have long been exploited to study the intervening interstellar medium (ISM) and circumgalactic medium (CGM) along the line of sight (e.g. Prochaska et al. 2007; Gatkine et al. 2019). To shine light on the origin of the narrow UV absorption lines in AT 2019qiz, we compare its spectrum with that of the GRB afterglow composite (Figure 13; Christensen et al. 2011). In AT 2019qiz, we derived a $N(\text{H I}) = 5 \times 10^{17} \text{ cm}^{-2}$ from the CoG analysis. This column density is consistent with a Lyman-limit system, where the clouds start to be dense enough to shield itself against the EUV background and remain neutral. GRB afterglow spectra, on the other hand, are often associated with a damped Ly α (DLA) system with a high neutral hydrogen column $\log(N(\text{H I})) > 20.3 \text{ cm}^{-2}$. The DLA line profile is dominated by the Voigt line profile that is very different from the Gaussian-like Ly α line profile in AT 2019qiz (Figure 13).

We observe stronger SiIV and CIV absorption in AT 2019qiz than in the GRB composite. The strength of the low-ionization species (Fe II and Mg II) are comparable to that in GRB afterglows. While the

$\text{N V } \lambda\lambda 1238, 1242$ absorption lines are well-detected in AT 2019qiz, they are harder to identify in GRB spectra due to blending with the red wing of $\text{Ly}\alpha$. The high ionization potential of N^{4+} (77 eV) makes it difficult to produce in stellar radiation fields. Galactic halo and disk do have N V absorption but none of them shows a column density $> 10^{14.5} \text{ cm}^{-2}$ (Prochaska et al. 2008 and references therein). Our measured N^{4+} column density of $\gtrsim 10^{15} \text{ cm}^{-2}$ thus likely indicates a hard ionizing spectrum, which can be attributed to the TDE accretion disk or in part the underlying weak AGN. The strong ionizing source may also explain the stronger Si IV , and C IV EW in AT 2019qiz than in the GRB composite. These high-ionization lines are likely to have formed in regions close to the SMBH rather than in the ISM. Our HST spectra cannot resolve fine-structure transitions such as Si II^* and Fe II^* in AT 2019qiz. In GRB afterglows, these fine-structure lines are thought to be produced by UV pumping and uniquely traces gas in the vicinity (100 pc–1kpc) of the burst (Prochaska 2006). We expect these lines to be detected in high S/N, high resolution TDE spectra since TDEs can also create a temporal UV radiation field.

Given the redshift of the absorption lines being close to the host redshift, we consider both circumnuclear gas and the bound stellar debris as the candidate absorbing system. In ASASSN-14li, Cenko et al. (2016) also detected narrow absorption lines with a width of $\approx 500 \text{ km s}^{-1}$ comparable to that in AT 2019qiz. However, the absorption lines in ASASSN-14li are blueshifted by $-(250 - 400) \text{ km s}^{-1}$ while the lines in AT 2019qiz do not appear to have a systemic velocity shift with respect to the host. The abundance pattern in ASASSN-14li is also very different. The low neutral hydrogen column of $\log(N(\text{H I})) < 14.2 \text{ cm}^{-2}$ is somewhat expected in host galaxies with an old stellar population (Cenko et al. 2016). However, ASASSN-14li lacks the low-ionization $\text{Mg II } \lambda\lambda 2796, 2803$ absorption that is commonly observed in cold ISM in the galaxy while having well-detected high-ionization lines. Together with the blueshift velocity being consistent with the outflow velocity measured from X-ray spectroscopy, Cenko et al. (2016) suggest that the low-velocity absorber is more likely the bound stellar debris on an elliptical orbit (Miller et al. 2015; Cenko et al. 2016).

The absorber in AT 2019qiz has several properties different from that in ASASSN-14li. The low-ionization species, such as Fe II and Mg II , are readily detected in AT 2019qiz with W_r comparable to those observed in GRB afterglow and QSO spectra, where the absorbing systems have been associated with galaxies. The likely lack of variability also counters the scenario in which the

absorbing gas is the bound stellar debris. Clumpiness, or bulk motion of the debris stream could easily alter the gas density and therefore lead to variability in the absorption lines on the fallback timescale $t_{\text{fallback}} \approx 40$ days. Therefore, we conclude that the absorption lines in AT2019 qiz are more likely to be probing the host ISM and circumnuclear gas instead of the stellar debris as in ASASSN-14li.

5. CONCLUSIONS

The early classification of AT 2019qiz and its proximity allow us to perform a detailed, multi-wavelength study of a TDE. Our UV and optical follow-up observations in both photometric and spectroscopic modes offer new insights for optically-selected TDEs. AT 2019qiz is located in a galaxy with a weak AGN, as evidenced by the line ratios on the BPT diagram. The evolution timescale and luminosity of AT 2019qiz is fast and faint, making it the intermediate event between iPTF16fnl and the rest of the TDE population.

Both the photosphere evolution and the BALs in the *HST* spectra strongly corroborate the outflow scenario in TDEs. We find the photosphere to be expanding at a constant velocity $v \sim 2400 \text{ km s}^{-1}$ before reaching t_{peak} . The early luminosity evolution in AT 2019qiz follows a power-law ($\propto t^2$), which is consistent with the predication of an expanding fireball. The BALs are detected in all three *HST* epochs with a decrease in outflow velocity from $15,000 \text{ km s}^{-1}$ to $10,000 \text{ km s}^{-1}$. This deceleration is expected as the mass fallback rate declines at later times.

The UV spectrum in the first *HST* epoch is unlike all the TDEs observed in the past as it contains both HiBAL and FeLoBAL features such as Al III and Fe II . The UV spectrum of AT 2019qiz resembles that of the SLSN Gaia16apd at maximum light more than that in any known FeLoBAL QSO. However, the broad $\text{Mg II } \lambda\lambda 2796, 2803$ doublet, which are readily found in both Gaia16apd and FeLoBAL QSOs, are not detected in AT 2019qiz. The disappearance of the FeLoBAL features in the later two *HST* epochs of AT 2019qiz is likely due to the thinning of the X-ray/EUV shielding material as the mass fallback/accretion rate decreases with time.

The detection of $\text{He II } \lambda 4686$ and the Balmer emission since the beginning of the monitoring up to day 89 makes AT 2019qiz a TDE-Bowen in the spectral classification scheme proposed by van Velzen et al. (2020a). We carefully studied the $\text{H}\alpha$ emission and found the line profile to be characterized by a very broad component with a FWHM of $\gtrsim 10^4 \text{ km s}^{-1}$ and a narrower component with FWHM $\sim 3,000 \text{ km s}^{-1}$ that only appeared after

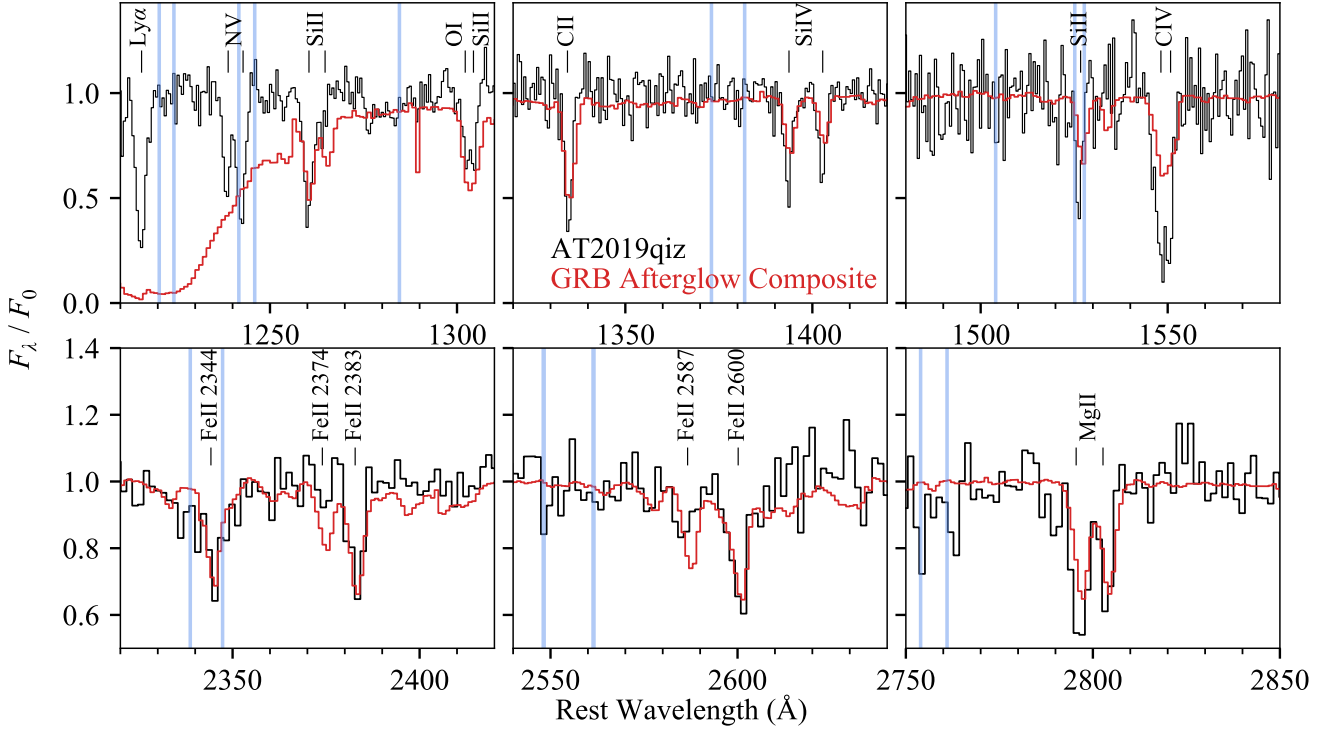


Figure 13. Comparison of the normalized spectrum of AT2019qiz (black) with the GRB composite from Christensen et al. (2011) (red). We indicate the wavelength for different transitions in the host galaxy rest-frame with black labels and possible contamination by foreground absorption ($z \approx 0$) with blue vertical lines.

$\Delta t \gtrsim 22$ days. The broad H α component narrows with time as observed in other TDEs and becomes more and more symmetric around the rest wavelength of H α . We inferred that the broad H α evolution is most likely to be driven by the outflow given the similar value of the H α line width and the BAL velocity, and the fact that the timing of decrease in broad H α width is seen to be coincident with the decrease in wind velocity probed the BALs.

We also analyzed the narrow absorption lines in the first *HST* spectrum and derived ionic column densities for several species using the CoG method. The measured Ly α EW corresponds to a Lyman-limit system, where the high-ionization species have stronger EWs and the low-ionization lines have similar EWs to those in GRB afterglows. We concluded that the narrow absorption lines are more likely to be probing the gas in the host galaxy rather than the bound stellar debris as in the case of ASASSN-14li. The UV spectra of AT 2019qiz demonstrates the potential of using TDEs to probe circumnuclear gas and ISM in TDE host galaxies. Future high S/N and high resolution UV spectra will allow us to resolve the fine structure lines produced by UV pumping in TDEs and study the gas in the vicinity of the SMBHs.

ACKNOWLEDGMENTS

T.H. is grateful to Ari Laor, Alexei Baskin, and Frederick Hamann for generously sharing their insightful thoughts on the UV spectral signatures in AT 2019qiz and providing BALQSO templates for comparison. She also thanks Dan Perley for helpful discussion on the similarities between AT 2019qiz and Gaia16apd. T.H. thanks Elizabeth Nance and John Debes for their help with scheduling the *HST* ToO observations.

This work is based on observations made with the NASA/ESA *Hubble Space Telescope* under program number GO-16026. Support for program GO-16026 was provided by NASA through a grant from the Space Telescope Science Institute, which is operated by the Association of Universities for Research in Astronomy, Inc., under NASA contract NAS 5-26555. This work makes use of observations from the Las Cumbres Observatory global telescope network following the approved program 2019B-0363. Support for TW-SH was provided by NASA through the NASA Hubble Fellowship grant #HST-HF2-51458.001-A awarded by the Space Telescope Science Institute, which is operated by the Association of Universities for Research in Astronomy, Inc., for NASA, under contract NAS5-26555. Parts of

this research were supported by the Australian Research Council Centre of Excellence for All Sky Astrophysics in 3 Dimensions (ASTRO 3D), through project number CE170100013. Research at Lick Observatory is partially supported by a generous gift from Google.

Some of the data presented herein were obtained at the W. M. Keck Observatory, which is operated as a scientific partnership among the California Institute of Technology, the University of California and the National Aeronautics and Space Administration. The Observatory was made possible by the generous financial support of the W. M. Keck Foundation. The authors wish to recognize and acknowledge the very significant cultural role and reverence that the summit of Maunakea has always had within the indigenous Hawaiian commu-

nity. We are most fortunate to have the opportunity to conduct observations from this mountain.

Based on observations obtained at the Southern Astrophysical Research (SOAR) telescope, which is a joint project of the Ministério da Ciência, Tecnologia, Inovações e Comunicações (MCTIC) do Brasil, the U.S. National Optical Astronomy Observatory (NOAO), the University of North Carolina at Chapel Hill (UNC), and Michigan State University (MSU).

This work includes data obtained with the Swope Telescope at Las Campanas Observatory, Chile, as part of the Swope Time Domain Key Project (PI: Piro, Co-Is: Drout, Phillips, Holoi, French, Cowperthwaite, Burns, Madore, Foley, Kilpatrick, Rojas-Bravo, Dimitriadis, Hsiao). The authors thank Swope Telescope observers Jorge Anais Vilchez, Abdo Campillay, Yilin Kong Riveros and Natalie Ulloa for collecting data presented in this paper.

REFERENCES

Alexander, K. D., Berger, E., Guillochon, J., Zauderer, B. A., & Williams, P. K. G. 2016, ApJL, 819, L25, doi: [10.3847/2041-8205/819/2/L25](https://doi.org/10.3847/2041-8205/819/2/L25)

Arcavi, I., Gal-Yam, A., Sullivan, M., et al. 2014, ApJ, 793, 38, doi: [10.1088/0004-637X/793/1/38](https://doi.org/10.1088/0004-637X/793/1/38)

Auchettl, K., Ramirez-Ruiz, E., & Guillochon, J. 2018, ApJ, 852, 37, doi: [10.3847/1538-4357/aa9b7c](https://doi.org/10.3847/1538-4357/aa9b7c)

Becker, A. 2015, HOTPANTS: High Order Transform of PSF ANd Template Subtraction, Astrophysics Source Code Library. <http://ascl.net/1504.004>

Bellm, E. C., Kulkarni, S. R., Graham, M. J., et al. 2019, PASP, 131, 018002, doi: [10.1088/1538-3873/aaecbe](https://doi.org/10.1088/1538-3873/aaecbe)

Blagorodnova, N., Cenko, S. B., Kulkarni, S. R., et al. 2019, ApJ, 873, 92, doi: [10.3847/1538-4357/ab04b0](https://doi.org/10.3847/1538-4357/ab04b0)

Bonnerot, C., Rossi, E. M., Lodato, G., & Price, D. J. 2016, MNRAS, 455, 2253, doi: [10.1093/mnras/stv2411](https://doi.org/10.1093/mnras/stv2411)

Brown, J. S., Kochanek, C. S., Holoi, T. W.-S., et al. 2018, MNRAS, 473, 1130, doi: [10.1093/mnras/stx2372](https://doi.org/10.1093/mnras/stx2372)

Cappellari, M. 2017, MNRAS, 466, 798, doi: [10.1093/mnras/stw3020](https://doi.org/10.1093/mnras/stw3020)

Cardelli, J. A., Clayton, G. C., & Mathis, J. S. 1989, ApJ, 345, 245, doi: [10.1086/167900](https://doi.org/10.1086/167900)

Cenko, S. B., Cucchiara, A., Roth, N., et al. 2016, ApJL, 818, L32, doi: [10.3847/2041-8205/818/2/L32](https://doi.org/10.3847/2041-8205/818/2/L32)

Chornock, R., Berger, E., Gezari, S., et al. 2014, ApJ, 780, 44, doi: [10.1088/0004-637X/780/1/44](https://doi.org/10.1088/0004-637X/780/1/44)

Christensen, L., Fynbo, J. P. U., Prochaska, J. X., et al. 2011, ApJ, 727, 73, doi: [10.1088/0004-637X/727/2/73](https://doi.org/10.1088/0004-637X/727/2/73)

Clemens, J. C., Crain, J. A., & Anderson, R. 2004, Society of Photo-Optical Instrumentation Engineers (SPIE) Conference Series, Vol. 5492, The Goodman spectrograph, ed. A. F. M. Moorwood & M. Iye, 331–340, doi: [10.1117/12.550069](https://doi.org/10.1117/12.550069)

Cutri, R. M., Skrutskie, M. F., van Dyk, S., et al. 2003, 2MASS All Sky Catalog of point sources.

Dai, L., McKinney, J. C., & Miller, M. C. 2015, ApJL, 812, L39, doi: [10.1088/2041-8205/812/2/L39](https://doi.org/10.1088/2041-8205/812/2/L39)

Dai, L., McKinney, J. C., Roth, N., Ramirez-Ruiz, E., & Miller, M. C. 2018, ApJL, 859, L20, doi: [10.3847/2041-8213/aab429](https://doi.org/10.3847/2041-8213/aab429)

Dimitriadis, G., Rojas-Bravo, C., Kilpatrick, C. D., et al. 2019, ApJL, 870, L14, doi: [10.3847/2041-8213/aaf9b1](https://doi.org/10.3847/2041-8213/aaf9b1)

Esquej, P., Saxton, R. D., Freyberg, M. J., et al. 2007, A&A, 462, L49, doi: [10.1051/0004-6361:20066072](https://doi.org/10.1051/0004-6361:20066072)

Evans, C. R., & Kochanek, C. S. 1989, ApJL, 346, L13, doi: [10.1086/185567](https://doi.org/10.1086/185567)

Flewelling, H. A., Magnier, E. A., Chambers, K. C., et al. 2016, arXiv e-prints. <https://arxiv.org/abs/1612.05243>

Foley, R. J., Papenkova, M. S., Swift, B. J., et al. 2003, PASP, 115, 1220, doi: [10.1086/378242](https://doi.org/10.1086/378242)

Frank, J., & Rees, M. J. 1976, MNRAS, 176, 633, doi: [10.1093/mnras/176.3.633](https://doi.org/10.1093/mnras/176.3.633)

French, K. D., Arcavi, I., Zabludoff, A. I., et al. 2020, ApJ, 891, 93, doi: [10.3847/1538-4357/ab7450](https://doi.org/10.3847/1538-4357/ab7450)

Gatkine, P., Veilleux, S., & Cucchiara, A. 2019, ApJ, 884, 66, doi: [10.3847/1538-4357/ab31ae](https://doi.org/10.3847/1538-4357/ab31ae)

Gehrels, N., Chincarini, G., Giommi, P., et al. 2004, ApJ, 611, 1005, doi: [10.1086/422091](https://doi.org/10.1086/422091)

Gezari, S., Chornock, R., Rest, A., et al. 2012, *Nature*, 485, 217, doi: [10.1038/nature10990](https://doi.org/10.1038/nature10990)

Guillochon, J., Nicholl, M., Villar, V. A., et al. 2018, *ApJS*, 236, 6, doi: [10.3847/1538-4365/aab761](https://doi.org/10.3847/1538-4365/aab761)

Guillochon, J., & Ramirez-Ruiz, E. 2013, *ApJ*, 767, 25, doi: [10.1088/0004-637X/767/1/25](https://doi.org/10.1088/0004-637X/767/1/25)

Hayasaki, K., Stone, N., & Loeb, A. 2016, *MNRAS*, 461, 3760, doi: [10.1093/mnras/stw1387](https://doi.org/10.1093/mnras/stw1387)

Hills, J. G. 1975, *Nature*, 254, 295, doi: [10.1038/254295a0](https://doi.org/10.1038/254295a0)

Holoien, T. W.-S., Prieto, J. L., Bersier, D., et al. 2014, *MNRAS*, 445, 3263, doi: [10.1093/mnras/stu1922](https://doi.org/10.1093/mnras/stu1922)

Holoien, T. W.-S., Kochanek, C. S., Prieto, J. L., et al. 2016, *MNRAS*, 455, 2918, doi: [10.1093/mnras/stv2486](https://doi.org/10.1093/mnras/stv2486)

Holoien, T. W.-S., Huber, M. E., Shappee, B. J., et al. 2019a, *ApJ*, 880, 120, doi: [10.3847/1538-4357/ab2ae1](https://doi.org/10.3847/1538-4357/ab2ae1)

Holoien, T. W. S., Vallely, P. J., Auchettl, K., et al. 2019b, *ApJ*, 883, 111, doi: [10.3847/1538-4357/ab3c66](https://doi.org/10.3847/1538-4357/ab3c66)

Holoien, T. W. S., Auchettl, K., Tucker, M. A., et al. 2020, *ApJ*, 898, 161, doi: [10.3847/1538-4357/ab9f3d](https://doi.org/10.3847/1538-4357/ab9f3d)

Hung, T., Gezari, S., Blagorodnova, N., et al. 2017, *ApJ*, 842, 29, doi: [10.3847/1538-4357/aa7337](https://doi.org/10.3847/1538-4357/aa7337)

Hung, T., Cenko, S. B., Roth, N., et al. 2019, *ApJ*, 879, 119, doi: [10.3847/1538-4357/ab24de](https://doi.org/10.3847/1538-4357/ab24de)

Hung, T., Foley, R. J., Ramirez-Ruiz, E., et al. 2020, *ApJ*, 903, 31, doi: [10.3847/1538-4357/abb606](https://doi.org/10.3847/1538-4357/abb606)

Jonker, P. G., Stone, N. C., Generozov, A., van Velzen, S., & Metzger, B. 2020, *ApJ*, 889, 166, doi: [10.3847/1538-4357/ab659c](https://doi.org/10.3847/1538-4357/ab659c)

Kara, E., Dai, L., Reynolds, C. S., & Kallman, T. 2018, *MNRAS*, 474, 3593, doi: [10.1093/mnras/stx3004](https://doi.org/10.1093/mnras/stx3004)

Kochanek, C. S. 2016, *MNRAS*, 458, 127, doi: [10.1093/mnras/stw267](https://doi.org/10.1093/mnras/stw267)

Komossa, S., & Bade, N. 1999, *A&A*, 343, 775

Komossa, S., & Greiner, J. 1999, *A&A*, 349, L45

Korista, K. T., Bautista, M. A., Arav, N., et al. 2008, *ApJ*, 688, 108, doi: [10.1086/592140](https://doi.org/10.1086/592140)

Law-Smith, J., Ramirez-Ruiz, E., Ellison, S. L., & Foley, R. J. 2017, *ApJ*, 850, 22, doi: [10.3847/1538-4357/aa94c7](https://doi.org/10.3847/1538-4357/aa94c7)

Law-Smith, J. A. P., Coulter, D. A., Guillochon, J., Mockler, B., & Ramirez-Ruiz, E. 2020, arXiv e-prints, arXiv:2007.10996. <https://arxiv.org/abs/2007.10996>

Levan, A. J., Tanvir, N. R., Cenko, S. B., et al. 2011, *Science*, 333, 199, doi: [10.1126/science.1207143](https://doi.org/10.1126/science.1207143)

Liu, F. K., Zhou, Z. Q., Cao, R., Ho, L. C., & Komossa, S. 2017, *MNRAS*, 472, L99, doi: [10.1093/mnrasl/slx147](https://doi.org/10.1093/mnrasl/slx147)

Lodato, G., Nayakshin, S., King, A. R., & Pringle, J. E. 2009, *MNRAS*, 398, 1392, doi: [10.1111/j.1365-2966.2009.15179.x](https://doi.org/10.1111/j.1365-2966.2009.15179.x)

Lodato, G., & Rossi, E. M. 2011, *MNRAS*, 410, 359, doi: [10.1111/j.1365-2966.2010.17448.x](https://doi.org/10.1111/j.1365-2966.2010.17448.x)

Loeb, A., & Ulmer, A. 1997, *ApJ*, 489, 573, doi: [10.1086/304814](https://doi.org/10.1086/304814)

Lu, W., & Bonnerot, C. 2020, *MNRAS*, 492, 686, doi: [10.1093/mnras/stz3405](https://doi.org/10.1093/mnras/stz3405)

Masci, F. J., Laher, R. R., Rusholme, B., et al. 2019, *PASP*, 131, 018003, doi: [10.1088/1538-3873/aae8ac](https://doi.org/10.1088/1538-3873/aae8ac)

Metzger, B. D., & Stone, N. C. 2016, *MNRAS*, 461, 948, doi: [10.1093/mnras/stw1394](https://doi.org/10.1093/mnras/stw1394)

Miller, J. M., Kaastra, J. S., Miller, M. C., et al. 2015, *Nature*, 526, 542, doi: [10.1038/nature15708](https://doi.org/10.1038/nature15708)

Miller, J. S., & Stone, R. P. S. 1993, *Lick Obs. Tech. Rep.*

Miller, M. C. 2015, *ApJ*, 805, 83, doi: [10.1088/0004-637X/805/1/83](https://doi.org/10.1088/0004-637X/805/1/83)

Mockler, B., Guillochon, J., & Ramirez-Ruiz, E. 2019, *ApJ*, 872, 151, doi: [10.3847/1538-4357/ab010f](https://doi.org/10.3847/1538-4357/ab010f)

Nicholl, M., Wevers, T., Oates, S. R., et al. 2020, *MNRAS*, 499, 482, doi: [10.1093/mnras/staa2824](https://doi.org/10.1093/mnras/staa2824)

Oke, J. B., Cohen, J. G., Carr, M., et al. 1995, *PASP*, 107, 375, doi: [10.1086/133562](https://doi.org/10.1086/133562)

Parkinson, E. J., Knigge, C., Long, K. S., et al. 2020, *MNRAS*, 494, 4914, doi: [10.1093/mnras/staa1060](https://doi.org/10.1093/mnras/staa1060)

Phinney, E. S. 1989, in *IAU Symposium*, Vol. 136, The Center of the Galaxy, ed. M. Morris, 543

Piran, T., Svirski, G., Krolik, J., Cheng, R. M., & Shiokawa, H. 2015, *ApJ*, 806, 164, doi: [10.1088/0004-637X/806/2/164](https://doi.org/10.1088/0004-637X/806/2/164)

Planck Collaboration, Aghanim, N., Akrami, Y., et al. 2020, *A&A*, 641, A6, doi: [10.1051/0004-6361/201833910](https://doi.org/10.1051/0004-6361/201833910)

Prochaska, J. X. 2006, *ApJ*, 650, 272, doi: [10.1086/507126](https://doi.org/10.1086/507126)

Prochaska, J. X., Chen, H.-W., Dessauges-Zavadsky, M., & Bloom, J. S. 2007, *ApJ*, 666, 267, doi: [10.1086/520042](https://doi.org/10.1086/520042)

Rees, M. J. 1988, *Nature*, 333, 523, doi: [10.1038/333523a0](https://doi.org/10.1038/333523a0)

Rest, A., Stubbs, C., Becker, A. C., et al. 2005, *ApJ*, 634, 1103, doi: [10.1086/497060](https://doi.org/10.1086/497060)

Rest, A., Scolnic, D., Foley, R. J., et al. 2014, *ApJ*, 795, 44, doi: [10.1088/0004-637X/795/1/44](https://doi.org/10.1088/0004-637X/795/1/44)

Roming, P. W. A., Kennedy, T. E., Mason, K. O., et al. 2005, *SSRv*, 120, 95, doi: [10.1007/s11214-005-5095-4](https://doi.org/10.1007/s11214-005-5095-4)

Roth, N., & Kasen, D. 2018, *ApJ*, 855, 54, doi: [10.3847/1538-4357/aaaec6](https://doi.org/10.3847/1538-4357/aaaec6)

Roth, N., Kasen, D., Guillochon, J., & Ramirez-Ruiz, E. 2016, *ApJ*, 827, 3, doi: [10.3847/0004-637X/827/1/3](https://doi.org/10.3847/0004-637X/827/1/3)

Schlafly, E. F., & Finkbeiner, D. P. 2011, *ApJ*, 737, 103, doi: [10.1088/0004-637X/737/2/103](https://doi.org/10.1088/0004-637X/737/2/103)

Shiokawa, H., Krolik, J. H., Cheng, R. M., Piran, T., & Noble, S. C. 2015, *ApJ*, 804, 85, doi: [10.1088/0004-637X/804/2/85](https://doi.org/10.1088/0004-637X/804/2/85)

Short, P., Nicholl, M., Lawrence, A., et al. 2020, arXiv e-prints, arXiv:2003.05470. <https://arxiv.org/abs/2003.05470>

Siebert, M. R., Strasburger, E., Rojas-Bravo, C., & Foley, R. J. 2019, Transient Name Server Classification Report, 2019-1921, 1

Silverman, J. M., Foley, R. J., Filippenko, A. V., et al. 2012, MNRAS, 425, 1789, doi: [10.1111/j.1365-2966.2012.21270.x](https://doi.org/10.1111/j.1365-2966.2012.21270.x)

Strubbe, L. E., & Quataert, E. 2009, MNRAS, 400, 2070, doi: [10.1111/j.1365-2966.2009.15599.x](https://doi.org/10.1111/j.1365-2966.2009.15599.x)

Svirski, G., Piran, T., & Krolik, J. 2017, MNRAS, doi: [10.1093/mnras/stx117](https://doi.org/10.1093/mnras/stx117)

van Velzen, S., Holoiu, T. W. S., Onori, F., Hung, T., & Arcavi, I. 2020a, arXiv e-prints, arXiv:2008.05461. <https://arxiv.org/abs/2008.05461>

van Velzen, S., Stone, N. C., Metzger, B. D., et al. 2018, arXiv e-prints, arXiv:1809.00003. <https://arxiv.org/abs/1809.00003>

van Velzen, S., Farrar, G. R., Gezari, S., et al. 2011, ApJ, 741, 73, doi: [10.1088/0004-637X/741/2/73](https://doi.org/10.1088/0004-637X/741/2/73)

van Velzen, S., Anderson, G. E., Stone, N. C., et al. 2016, Science, 351, 62, doi: [10.1126/science.aad1182](https://doi.org/10.1126/science.aad1182)

van Velzen, S., Gezari, S., Cenko, S. B., et al. 2019, ApJ, 872, 198, doi: [10.3847/1538-4357/aafe0c](https://doi.org/10.3847/1538-4357/aafe0c)

van Velzen, S., Gezari, S., Hammerstein, E., et al. 2020b, arXiv e-prints, arXiv:2001.01409. <https://arxiv.org/abs/2001.01409>

Wang, J., Xu, D., & Wei, J. 2017, Frontiers in Astronomy and Space Sciences, 4, 40, doi: [10.3389/fspas.2017.00040](https://doi.org/10.3389/fspas.2017.00040)

Wu, S., Coughlin, E. R., & Nixon, C. 2018, MNRAS, 478, 3016, doi: [10.1093/mnras/sty971](https://doi.org/10.1093/mnras/sty971)

Xiao, T., Barth, A. J., Greene, J. E., et al. 2011, ApJ, 739, 28, doi: [10.1088/0004-637X/739/1/28](https://doi.org/10.1088/0004-637X/739/1/28)

Yan, L., Quimby, R., Gal-Yam, A., et al. 2017, ApJ, 840, 57, doi: [10.3847/1538-4357/aa6b02](https://doi.org/10.3847/1538-4357/aa6b02)

Yang, C., Wang, T., Ferland, G. J., et al. 2017, ApJ, 846, 150, doi: [10.3847/1538-4357/aa8598](https://doi.org/10.3847/1538-4357/aa8598)